

Dynamic Modeling, Stability, and Control of Power Systems with Distributed Energy Resources

Tomonori Sadamoto¹, Aranya Chakraborty², Takayuki Ishizaki¹, Jun-ichi Imura¹

Abstract

This article presents a suite of new control designs for next-generation electric smart grids. The future grid will consist of thousands of non-conventional renewable generation sources such as wind, solar, and energy storage. These new components are collectively referred to as distributed energy resources (DER). The article presents a comprehensive list of dynamic models for DERs, and shows their coupling with the conventional generators and loads. It then presents several innovative control designs that can be used for facilitating large-scale DER integration. Ideas from decentralized retrofit control and distributed sparsity-promoting optimal control are used for developing these designs, followed by illustrations on an IEEE power system test model.

I. INTRODUCTION

Significant infrastructural changes are currently being implemented on power system networks around the world by maximizing the penetration of renewable energy, by installing new transmission lines, by adding flexible loads, by promoting independence in power production by disintegrating the grid into micro-grids, and so on [1]. The shift of energy supply from large central generating stations to smaller producers such as wind farms, solar photovoltaic (PV) farms, roof-top PVs, and energy storage systems, collectively known as Distributed Energy Resources (DERs) or Inverter-Based Resources (IBRs), is accelerating at a very rapid pace. Hundreds of power electronic devices are being added, creating hundreds of new control points in the grid. This addition is complimented by an equal progress in sensing technology, whereby high-precision, high sampling-rate, GPS-synchronized dynamic measurements of voltages and currents are now available from sensors such as Phasor Measurement Units (PMUs) [2]. With all these transformational changes happening in the grid, operators are inclining to explore new control methods that go far beyond how the grid is controlled today. A list of these changes is summarized in Table I.

In the current state-of-art, power system controllers, especially the ones that are responsible for transient stability and power oscillation damping, are all operated in a decentralized and uncoordinated fashion using local output feedback only. A survey of these controllers is provided in Appendix A. With rapid modernization of the grid, these local controllers, however, will not be tenable over the long-term. Instead, system-wide coordinated controllers will become essential. Such controllers where signals measured at one part of the grid are communicated to other remote parts for feedback are called wide-area controllers [3].

Wide-area control (WAC) alone, however, will not be enough either. It may improve the stability and dynamics performance of the legacy system, but will not be able to keep up with the unpredictable rate at which DERs are being added to the grid. Every time a new DER is added it will be almost impossible for an operator to retune all the wide-area control gains to accommodate the change in dynamics. DERs have high variability and intermittency, and need to be operated in a plug-and-play fashion. Accordingly their controllers need to be local, decentralized, and modular in both design and implementation. In other words, neither should the design of one DER controller depend on that of another nor should either of these two controllers need to be updated when a third DER is added in the future. The overall control architecture for the future grid needs to be a combination of these *decentralized* plug-and-play DER controllers and *distributed* wide-area controllers.

¹ Department of Systems and Control Engineering, Graduate School of Engineering, Tokyo Institute of Technology; 2-12-1, Meguro, Tokyo, Japan. {sadamoto, ishizaki, imura}@sc.e.titech.ac.jp

² Electrical & Computer Engineering, North Carolina State University; Raleigh, NC 27695. achakra2@ncsu.edu

The objective of this article is twofold. The first objective is to present a suite of control methods, for developing this combined control architecture. The presentation will be based on recent results reported by the authors in [4] and [5]. For brevity, the discussion will be limited to only one particular application - namely, adding damping to the oscillations in power flows after both small and large disturbances, also called *power oscillation damping* (POD) [6]. POD is one of the most critical real-time control problems in today's power grid, and its importance is only going to increase with DER integration. The applicability of the design, however, go far beyond just POD to many other grid control problems such as frequency control, voltage control, and congestion relief. Efficacy of the methods for enhancing transient stability as a bonus application will be illustrated via simulations. While many papers on decentralized DER control and distributed wide-area control exist in the literature (surveys on these two control methods are given in Appendix B and C, respectively), very few have studied the simultaneous use of both. Moreover, most DER controllers reported so far lack the modularity and plug-and-play characteristic explained above. The control methods presented in this article address all of these challenges. The second objective is to present a comprehensive list of mathematical models of the various components of a power grid ranging from synchronous generators, their internal controllers, loads, wind and solar farms, batteries to the power electronic device interfaces and associated control mechanisms for each of these components. While these models are individually well-cited in the literature, very few references so far have collected all of them together to understand the holistic dynamic behavior of an entire grid. The three main contributions of the article are summarized as follows:

- Present an end-to-end differential-algebraic model of a power system in its entirety - including, synchronous generators, wind farms, solar farms, energy storages, power electronic converters, and controllers for each device.
- Show how DERs and power electronic devices affect small-signal stability and dynamic performance of the grid.
- Present a two-layer control architecture for tomorrow's grid, where one layer consists of decentralized plug-and-play controllers for power electronic converter control of DERs, and another layer consists of system-wide distributed controllers actuated through the generators.

The rest of the article is organized as follows. The next section describes the dynamic model of a power system, integrated with different types of DERs. A general framework for modeling is provided first, followed by details of each individual component model. The section III demonstrates the impacts of DERs on power system dynamics through numerical simulations. Motivated by these simulation results, the section IV shows newly-developed decentralized DER control laws using the idea of *retrofit control* [4], as well as distributed wide-area controllers for damping of low frequency oscillations using sparse optimal control [5]. The effectiveness of this combined control strategy is demonstrated on the IEEE 68-bus power system with wind and solar farms. The article concludes with a list of open research problems.

II. POWER SYSTEM MODELS

First, the dynamic models of the four core components of a power system are developed - namely, generation, transmission, load, and energy storage. The generating units are classified into conventional power plants and DERs such as wind generators and PV generators. Each model follows from first-principles of physics. Note that in reality a generation facility, whether that be conventional generation or wind/solar generation, and energy storage facilities contain many generating units and storage devices inside them. In the following, the terms *generator*, *wind farm*, *solar farm*, and *energy storage system* are used to refer to an aggregate of those individual units representing the overall facility. Similarly, the term *load* is used to refer to an aggregate of all consumers inside the associated demand area. Each aggregated unit comes with its own individual bus, such as a generator bus or a load bus. The buses are connected to each other through a network of power transmission lines. The power system may also contain buses where no generator, wind/solar farm, load, or energy storage system is connected. These buses are called non-unit buses. The term *component* is used to refer to either a unit with its bus or the non-unit bus. An example of these connected components is shown in Figure 1.

TABLE I
TRANSITIONS IN POWER GRID INFRASTRUCTURE

	Today	Tomorrow
Generation units	Synchronous generators	+ Renewable generation with power electronic converters, storage devices
Load Mechanisms	Conventional consumers	Prosumers (Producers + Consumers), PHEVs, smart buildings, load-side decision-making.
Transmission	Moderately dense, one-directional power flow	More dense, bi-directional power flow
Control	Local control (AVR, PSS, FACTS, PI)	System-wide control, plug-and-play control
Controller Design	Model-driven, seldom retuned	Measurement-driven, adaptive, reconfigurable
Monitoring System	Slow sensing (SCADA)	Fast sensing (WAMS based on PMUs)
Communication	Low-bandwidth legacy communication	High-speed communication, more importance on cyber-security and privacy
Data Processing	Offline processing, low volumes of data	Real-time processing using cloud computing, massive volumes of data

TABLE II
ACRONYMS USED IN THIS ARTICLE AND THEIR COMPLETE EXPRESSIONS.

Acronyms	Complete expression
PV	Photovoltaic
DER	Distributed Energy Resources
IBR	Inverter-Based Resources
FACTS	Flexible Alternating Current Transmission System
PHEV	Plug-in Hybrid Electric Vehicle
SCADA	Supervisory Control And Data Acquisition
WAMS	Wide Area Monitoring Systems
GPS	Global Positioning System
PMU	Phasor Measurement Unit
WAC	Wide Area Control
POD	Power Oscillation Damping
AVR	Automatic Voltage Regulator
PSS	Power System Stabilizer
DFIG	Doubly-Fed Induction Generator
B2B	Back-to-Back
RSC	Rotor-Side Converter
GSC	Grid-Side Converter
MPP	Maximum Power Point
LFC	Load Frequency Control

TABLE III
NOMENCLATURE FOR POWER SYSTEM MODELS. THE TIE-LINE PARAMETERS FOR CONSTRUCTING \mathbf{Y} OF THE IEEE 68-BUS POWER MODEL, WHICH IS A BENCHMARK MODEL USED IN THE SIMULATION, ARE AVAILABLE IN [7]. ALL VARIABLES ARE CONSIDERED TO BE IN PER UNIT UNLESS OTHERWISE STATED.

Symbol	Numerical value	Description
$\bar{\omega}$	120 π	base angular speed for a 60 Hz power system. Unit of $\bar{\omega}$ is rad/sec.
N		number of buses
$\mathbf{V}_k \in \mathbb{C}$		k -th bus voltage
P_k, Q_k		active and reactive power injected from the k -th component
x_k		state of the k -th component
u_k		control input of the k -th component
α_k		model parameter depending on operating point
$\mathbf{Y} \in \mathbb{C}^{N \times N}$		admittance matrix
$\mathbb{N}_G, \mathbb{N}_L, \mathbb{N}_W, \mathbb{N}_S,$ $\mathbb{N}_E, \mathbb{N}_N$		index set of the buses connecting to generators, loads, wind farms, solar farms, energy storages, and that of non-unit buses. These sets are disjoint, and $\mathbb{N}_G \cup \mathbb{N}_L \cup \mathbb{N}_W \cup \mathbb{N}_S \cup \mathbb{N}_E \cup \mathbb{N}_N = \{1, \dots, N\}$

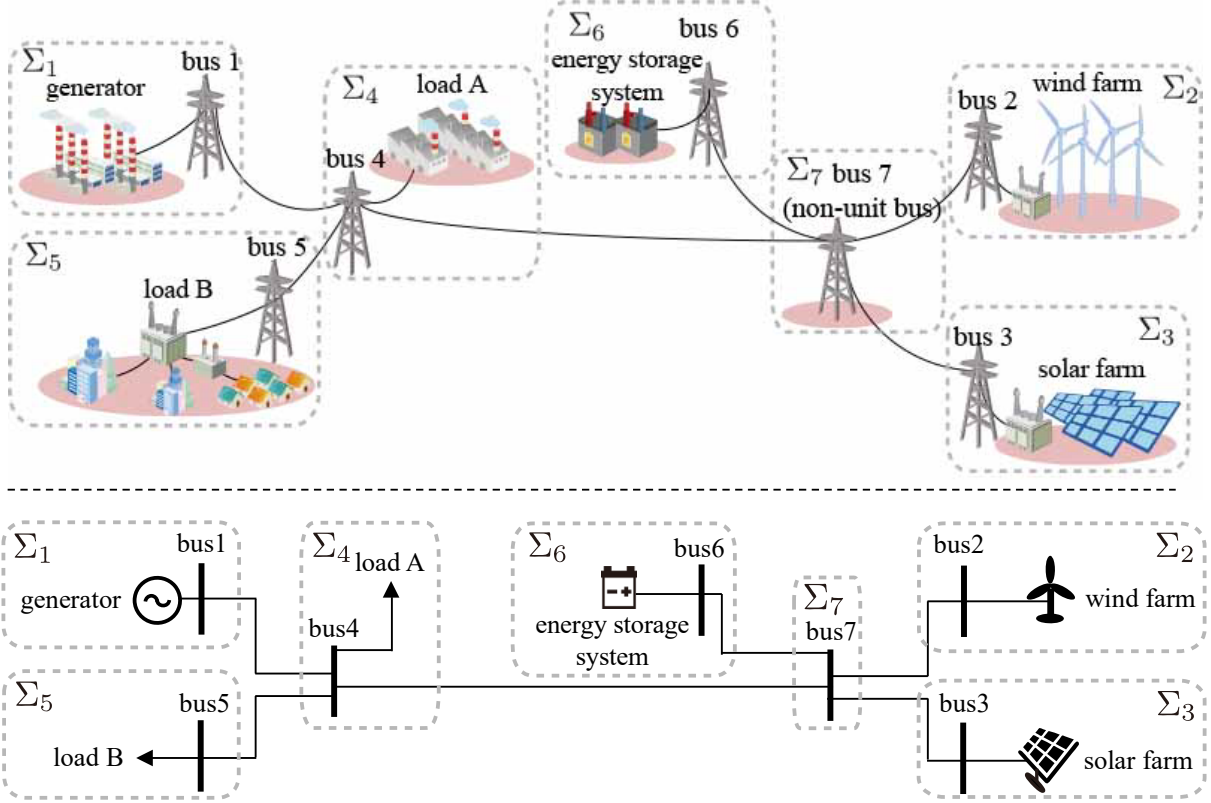


Fig. 1. (Top) Illustrative example of a power system. (Bottom) Schematic diagram of the model.

As will be shown in the following, a general form for the dynamic model of the k -th component of a power system, whether that component be a generator, load, storage, wind farm, or solar farm, can be written as

$$\Sigma_k : \begin{cases} \dot{x}_k &= f_k(x_k, \mathbf{V}_k, u_k; \alpha_k), \\ P_k + jQ_k &= g_k(x_k, \mathbf{V}_k; \alpha_k), \end{cases} \quad (1)$$

for $k \in \{1, \dots, N\}$. The nomenclature of this model is summarized in Table III. Details of the two functions $f_k(\cdot, \cdot, \cdot; \cdot)$ and $g_k(\cdot, \cdot; \cdot)$ for each component will be described shortly. Throughout the article, complex variables will be written in bold fonts (for example \mathbf{V}). All symbols with superscript \star will denote setpoints.

The N components are interconnected by a transmission network. Let $\mathbf{Y} \in \mathbb{C}^{N \times N}$ denote the admittance matrix of the network (for details of the construction of this matrix, please see Appendix C). The power balance across the transmission lines follows from Kirchhoff's laws as

$$0 = (\mathbf{Y}\mathbf{V}_{1:N})^* \circ \mathbf{V}_{1:N} - (P_{1:N} + jQ_{1:N}), \quad (2)$$

where \circ is the element-wise multiplication, $*$ is the element-wise complex conjugate operator, $\mathbf{V}_{1:N}$, $P_{1:N}$, and $Q_{1:N}$ are the stacked representations of \mathbf{V}_k , P_k and Q_k for $k \in \{1, \dots, N\}$. From (2), $\mathbf{V}_{1:N}$ is determined for a given $P_{1:N}$ and $Q_{1:N}$. The overall dynamics of a power system can be described by the combination of (1) and (2). A signal-flow diagram of this model is shown in Figure 2.

The power system model (1)-(2) is operated around its equilibrium. This is determined as follows. The steady-state value of x_k , \mathbf{V}_k , P_k , and Q_k , and parameter α_k in (1) must satisfy

$$\begin{cases} 0 &= f_k(x_k^*, \mathbf{V}_k^*, 0; \alpha_k), \\ P_k^* + jQ_k^* &= g_k(x_k^*, \mathbf{V}_k^*; \alpha_k), \end{cases} \quad (3)$$

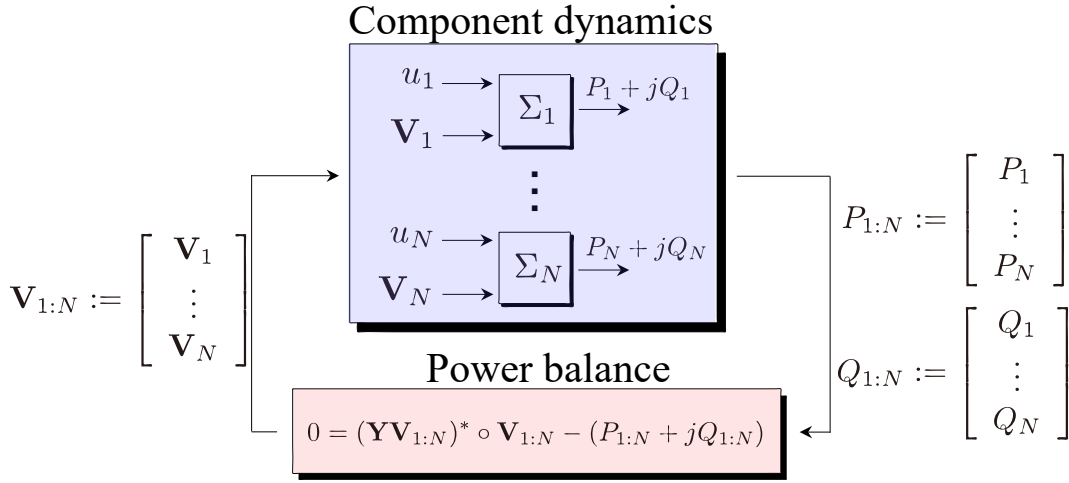


Fig. 2. Signal-flow diagram of power system model (1) and (2)

and (2). The steady-state value of u_k is assumed to be zero without loss of generality. A standard procedure for finding the steady-state values consists of two steps: *power flow calculation* and *initialization*, which are summarized as follows.

Power Flow Calculation:

Find $\mathbf{V}_{1:N}^*$, $P_{1:N}^*$, and $Q_{1:N}^*$ satisfying (2) and other constraints for individual components (see Appendix D for the details of these constraints).

Initialization:

For $k \in \{1, \dots, N\}$, given \mathbf{V}_k^* , P_k^* , and Q_k^* , find x_k^* and α_k satisfying (3). These solutions then serve as the initial conditions for the dynamic model (1)-(2) for any incoming contingency.

Note that there exist an infinite number of solutions satisfying (2). However, \mathbf{V}_k , P_k and Q_k of some of the components are either known a priori or specified by economic dispatch [6]. The details of this are described in Appendix D. Once the steady-state values of $\mathbf{V}_{1:N}$, $P_{1:N}$ and $Q_{1:N}$ are obtained, in the second step the setpoints x_k^* and α_k of the k -th component can be computed independently. The details of this initialization step will be described later in each subsection describing the detailed dynamics of the components. The uniqueness of the solution (x_k^*, α_k) satisfying (3) under a given triple $(\mathbf{V}_k^*, P_k^*, Q_k^*)$ depends on the component itself. In fact, the equilibria for the generators, loads, and non-unit buses are unique, but those for wind farms, solar farms, and energy storage systems are not. The details of this uniqueness property will also be described in the following subsections.

Next, the state-space models of generators, loads, energy storage systems, wind farms, solar farms, and non-unit buses, conforming to the structure in (1), are derived. For easier understanding, each subsection starts with a qualitative description of the respective component model followed by its state-space representation. Some parts may refer to equations that appear later in the text. To simplify the notation, the subscript k is omitted unless otherwise stated.

A. Generators

A generator consists of a synchronous machine, an energy supply system (or a prime-mover), and an excitation system [6]. The excitation system induces currents in the excitation winding, and thereby magnetizes the rotor. The prime-mover generates mechanical power to rotate the rotor in this magnetic field. The synchronous machine converts the mechanical power to electrical power, which is transmitted to the rest of the grid. The dynamics of the prime-mover are usually ignored because of their slow time constant [8], [9], [10].

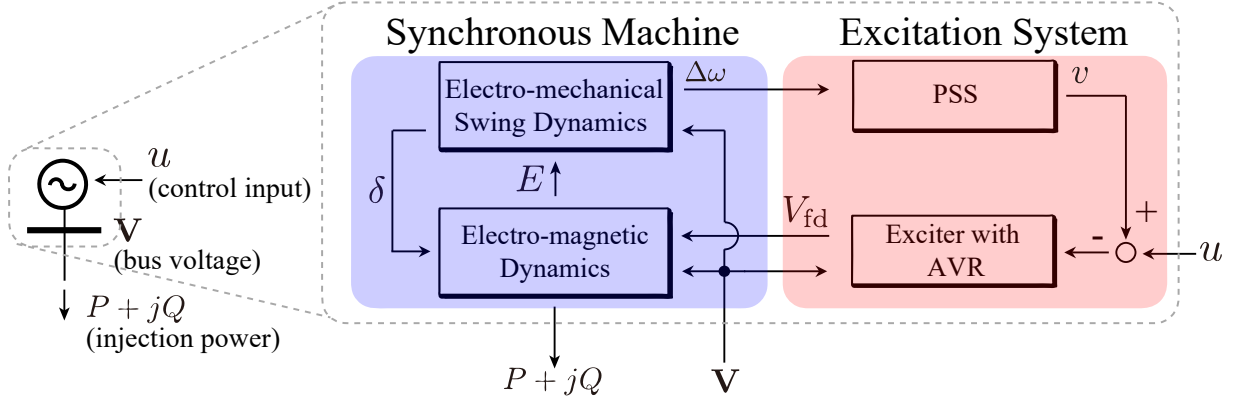


Fig. 3. Signal-flow diagram of the model of a generator with its terminal bus, where the constant signals P_m^* , V_{fd}^* , and $|\mathbf{V}|^*$ are omitted.

1) *Synchronous Machine*: While various types of synchronous machine models are available in the literature (for example see [6]), in this article a well-known model called the *one-axis model* or *flux-decay model* is used. This model consists of the electro-mechanical swing dynamics (4) and the electro-magnetic voltage dynamics (5). For simplicity, the mechanical power P_m^* in (4) is assumed to be constant.

2) *Excitation System*: Typically, the excitation system consists of an exciter, an Automatic Voltage Regulator (AVR) that regulates the generator voltage magnitude to its setpoint value, and a Power System Stabilizer (PSS) that ensures the power system stability. The exciter with AVR is modeled as (6), where u is a control input representing an additional voltage reference signal to the AVR. The PSS is taken as a typical speed-feedback type controller which consists of two stage lead-lag compensators and one highpass washout filter [11].

The state-space representation of the overall generator model can be written as follows (definitions of $\bar{\omega}$, \mathbf{V} , $P + jQ$, u are given in Table III while those of the other symbols are provided in Table IV):

Synchronous machine:

- Electro-mechanical swing dynamics:

$$\begin{cases} \dot{\delta} = \bar{\omega}\Delta\omega, \\ \Delta\dot{\omega} = \frac{1}{M} \left(P_m^* - d\Delta\omega - \frac{|\mathbf{V}|E}{X_d'} \sin(\delta - \angle\mathbf{V}) + \frac{|\mathbf{V}|^2}{2} \left(\frac{1}{X_d'} - \frac{1}{X_q} \right) \sin(2\delta - 2\angle\mathbf{V}) \right). \end{cases} \quad (4)$$

- Electro-magnetic dynamics:

$$\begin{cases} \dot{E} = \frac{1}{\tau_{do}} \left(-\frac{X_d}{X_d'} E + \left(\frac{X_d}{X_d'} - 1 \right) |\mathbf{V}| \cos(\delta - \angle\mathbf{V}) + V_{fd} \right), \\ P + jQ = \frac{E|\mathbf{V}|}{X_d'} \sin(\delta - \angle\mathbf{V}) - \frac{|\mathbf{V}|^2}{2} \left(\frac{1}{X_d'} - \frac{1}{X_q} \right) \sin(2\delta - 2\angle\mathbf{V}) \\ \quad + j \left(\frac{E|\mathbf{V}|}{X_d'} \cos(\delta - \angle\mathbf{V}) - |\mathbf{V}|^2 \left(\frac{\sin^2(\delta - \angle\mathbf{V})}{X_q} + \frac{\cos^2(\delta - \angle\mathbf{V})}{X_d'} \right) \right). \end{cases} \quad (5)$$

Excitation System:

- Exciter with AVR:

$$\dot{V}_{fd} = \frac{1}{\tau_e} (-V_{fd} + V_{fd}^* + V_{ef}), \quad V_{ef} = K_a (|\mathbf{V}| - |\mathbf{V}|^* - v + u), \quad (6)$$

where $|\mathbf{V}|^*$ represents the setpoint of $|\mathbf{V}|$.

- PSS:

$$\dot{\zeta} = A_{pss}\zeta + B_{pss}\Delta\omega, \quad v = C_{pss}\zeta + D_{pss}\Delta\omega, \quad (7)$$

TABLE IV

NOMENCLATURE FOR GENERATOR MODEL. THE VALUES OF THE SYNCHRONOUS MACHINE PARAMETERS BELOW ARE TYPICAL, AND RATED AT GENERATOR CAPACITY. THE PARAMETERS FOR THE IEEE 68-BUS TEST SYSTEM, WHICH IS A BENCHMARK POWER SYSTEM MODEL USED LATER IN THIS ARTICLE, ARE AVAILABLE IN [7].

Symbol	Numerical value	Description
δ		rotor angle relative to the frame rotating at $\bar{\omega}$. Unit of δ is (rad)
$\Delta\omega$		frequency deviation, that is, rotor angular velocity relative to $\bar{\omega}$
E		q-axis voltage behind transient reactance X'_d
V_{fd}		field voltage
$\zeta \in \mathbb{R}^3$		PSS state
V_{ef}		exciter field voltage
v		PSS output
u		additional voltage reference to AVR
M	30	inertia constant (sec)
d	0.1	damping coefficient
τ_{do}	0.1	d-axis transient open-circuit time constant (sec)
X_d, X_q	1.8	d- and q-axis synchronous reactance
X'_d	0.3	d-axis transient reactance
P_m^*	8.0	steady-state mechanical power
τ_e	0.05	time constant of exciter (sec)
K_a	20	AVR gain
K_{pss}	150	PSS gain
V_{fd}^*	1.0	setpoints for the field voltage
$ \mathbf{V} ^*$	1.0	setpoints for the bus voltage magnitude
τ_{pss}	10	washout filter time constant (sec)
τ_{L1}, τ'_{L1}	0.02, 0.07	lead-lag time constants of the first stage of PSS (sec)
τ_{L2}, τ'_{L2}	0.02, 0.07	lead-lag time constants of the second stage of PSS (sec)

where

$$A_{pss} = \begin{bmatrix} -\frac{1}{\tau_{pss}} & 0 & 0 \\ -\frac{K_{pss}}{\tau_{pss}\tau_{L1}}(1 - \frac{\tau'_{L1}}{\tau_{L1}}) & -\frac{1}{\tau_{L1}} & 0 \\ -\frac{K_{pss}\tau'_{L1}}{\tau_{pss}\tau_{L1}\tau_{L2}}(1 - \frac{\tau'_{L2}}{\tau_{L2}}) & \frac{1}{\tau_{L2}}(1 - \frac{\tau'_{L2}}{\tau_{L2}}) & -\frac{1}{\tau_{L2}} \end{bmatrix}, \quad B_{pss} = \begin{bmatrix} \frac{1}{\tau_{pss}} \\ \frac{K_{pss}}{\tau_{pss}\tau_{L1}}(1 - \frac{\tau'_{L1}}{\tau_{L1}}) \\ \frac{K_{pss}\tau'_{L1}}{\tau_{pss}\tau_{L1}\tau_{L2}}(1 - \frac{\tau'_{L2}}{\tau_{L2}}) \end{bmatrix}, \quad (8)$$

$$C_{pss} = \begin{bmatrix} -\frac{K_{pss}\tau'_{L1}\tau'_{L2}}{\tau_{pss}\tau_{L1}\tau_{L2}} & \frac{\tau'_{L2}}{\tau_{L2}} & 1 \end{bmatrix}, \quad D_{pss} = \frac{K_{pss}\tau'_{L1}\tau'_{L2}}{\tau_{pss}\tau_{L1}\tau_{L2}}.$$

Therefore, for $k \in \mathbb{N}_G$, the model of the generator at the k -th bus can be written in the form of (1) with

$$x_k := [\delta_k, \Delta\omega_k, E_k, V_{fd,k}, \zeta_k^T]^T \in \mathbb{R}^7, \quad \alpha_k := [P_{m,k}^*, V_{fd,k}^*, |\mathbf{V}_k|^*]^T \in \mathbb{R}^3, \quad (9)$$

and $f_k(\cdot, \cdot, \cdot; \cdot)$ and $g_k(\cdot, \cdot; \cdot)$ in (1) follow from (4)-(8). The signal-flow diagram of this model is shown in Figure 3. For a given triple $(\mathbf{V}_k^*, P_k^*, Q_k^*)$, the pair (x_k^*, α_k) satisfying (3) is uniquely determined as $x_k^* = [\delta_k^*, 0, E_k^*, V_{fd,k}^*, 0, 0, 0]^T$ and α_k in (9) with $P_{m,k}^* = P_k^*$ where

$$\delta_k^* = \angle \mathbf{V}_k^* + \arctan \left(\frac{P_k^*}{Q_k^* + \frac{|\mathbf{V}_k|^*{}^2}{X_{q,k}}} \right), \quad V_{fd,k}^* = \frac{X_{d,k}}{X'_{d,k}} E_k^* - \left(\frac{X_{d,k}}{X'_{d,k}} - 1 \right) |\mathbf{V}_k|^* \cos(\delta_k^* - \angle \mathbf{V}_k^*), \quad (10)$$

$$E_k^* = \frac{|\mathbf{V}_k|^*{}^4 + Q_k^{*2} X'_{d,k} X_{q,k} + Q_k^* |\mathbf{V}_k|^*{}^2 X'_{d,k} + Q_k^* |\mathbf{V}_k|^*{}^2 X_{q,k} + P_k^{*2} X'_{d,k} X_{q,k}}{|\mathbf{V}_k|^* \sqrt{P_k^{*2} X_{q,k}^2 + Q_k^{*2} X_{q,k}^2 + 2Q_k^* |\mathbf{V}_k|^*{}^2 X_{q,k} + |\mathbf{V}_k|^*{}^4}}.$$

Remark 1: Relationships between the one-axis model (4)-(5) and some other standard models of synchronous generators are shown in Appendix E.

B. Non-unit Buses

Non-unit buses are simply modeled by the Kirchhoff's power balance law, namely for $k \in \mathbb{N}_N$,

$$P_k + jQ_k = 0. \quad (11)$$

In reference to (1) this means x_k , u_k , and α_k are empty vectors.

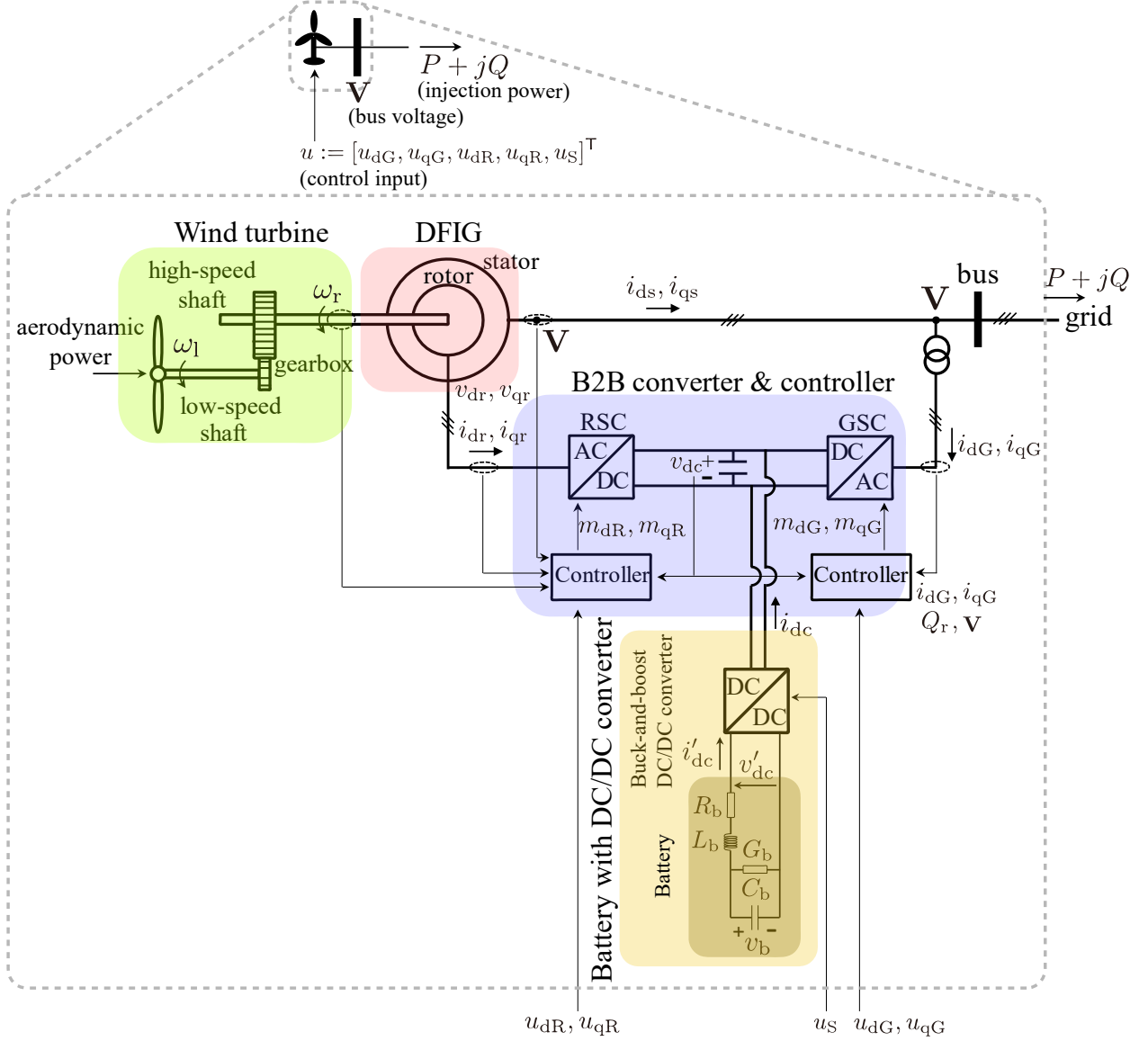


Fig. 4. Physical structure of the model of a wind farm with its terminal bus

C. Loads

Loads are commonly modeled by algebraic power balance equations, although extensive literature also exists for dynamic loads (for example, see [12], [13]). The well-known static load models are:

$$\text{constant impedance model:} \quad P + jQ = (\bar{z}^{-1} \mathbf{V})^* \mathbf{V}, \quad (12)$$

$$\text{constant current model:} \quad P + jQ = \bar{\mathbf{i}}^* \mathbf{V}, \quad (13)$$

$$\text{constant power model:} \quad P + jQ = \bar{P} + j\bar{Q}, \quad (14)$$

where $*$ is the complex conjugate operator, $\bar{z} \in \mathbb{C}$, $\bar{\mathbf{i}} \in \mathbb{C}$, and $\bar{P} + j\bar{Q} \in \mathbb{C}$ are constant. Therefore, for $k \in \mathbb{N}_L$, in reference to (1) a load at the k -th bus can be represented by x_k and u_k being empty vectors, α_k being either \bar{z}_k , $\bar{\mathbf{i}}_k$, or $\bar{P}_k + j\bar{Q}_k$, and the output equation being either (12), (13) or (14). For the simulations later in this article, constant impedance loads will be used. For a given triple $(\mathbf{V}_k^*, P_k^*, Q_k^*)$, the load impedance \bar{z}_k will be uniquely calculated such that $P_k^* + jQ_k^* = (\bar{z}_k^{-1} \mathbf{V}_k^*)^* \mathbf{V}_k^*$.

D. Wind Farms

A wind farm model typically consists of a wind turbine, a doubly-fed induction generator (DFIG), and a back-to-back (B2B) converter with associated controllers. A battery with DC/DC converter can be added

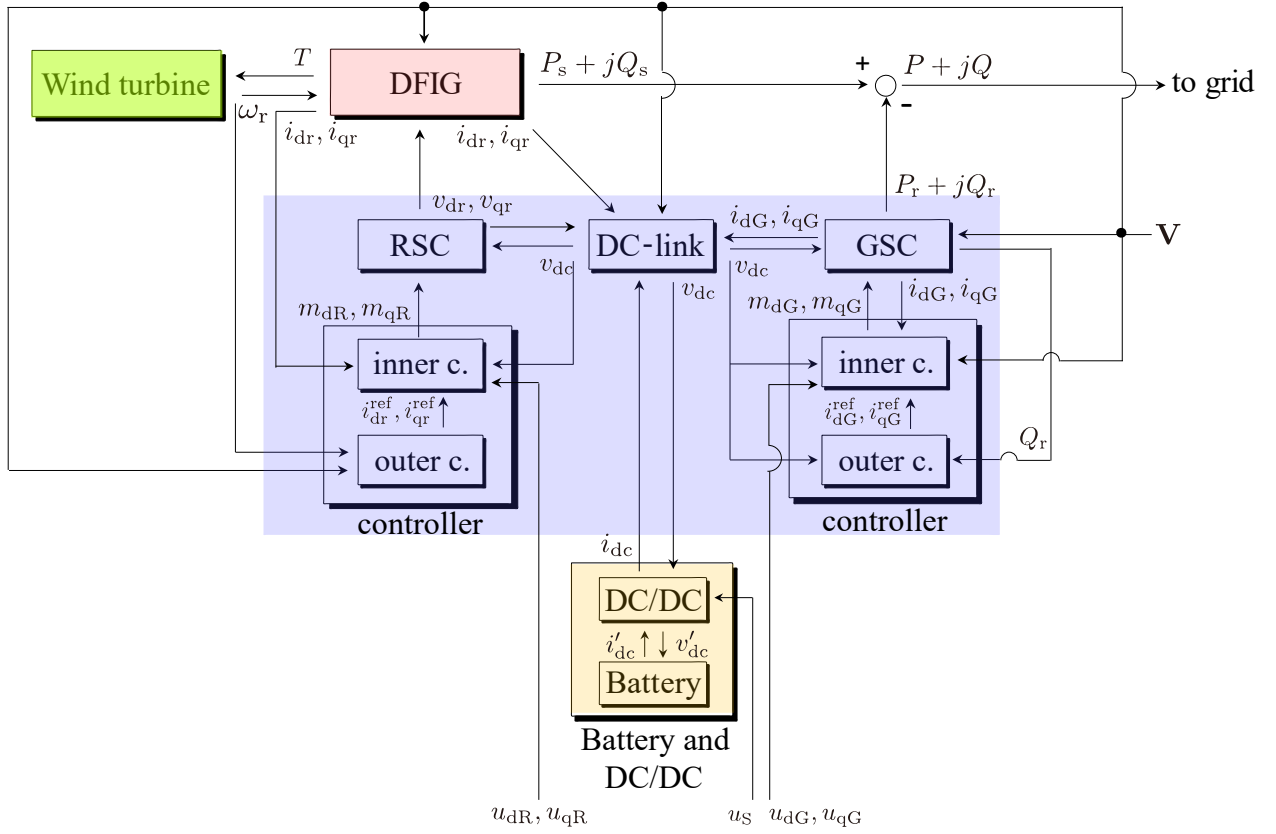


Fig. 5. Signal-flow diagram of the model of a wind farm with its terminal bus, where constant signals P_a , v_{dc}^* , Q_r^* , $|\mathbf{V}|^*$, ω_r^* are omitted.

to the B2B converter if needed. Figure 4 shows the physical architecture of a wind farm with its bus while Figure 5 shows a signal-flow diagram of the model. When the battery is not connected, the current i_{dc} in Figure 4 is regarded as zero. The symbols for the wind farm model are listed in Table V.

1) *Wind Turbine*: The wind turbine, as shown in Figure 4, converts aerodynamic power coming from the wind to mechanical power that is transmitted to the DFIG. The turbine is typically modeled as a one-inertia or two-inertia model (the latter is followed in this article) consisting of a low-speed shaft, a high-speed shaft, and a gearbox [14]. For simplicity, the aerodynamic power P_a in the two-inertia dynamics (16) is assumed to be constant as wind speeds usually change slowly.

2) *Doubly-Fed Induction Generator (DFIG)*: The DFIG shown in Figure 4 converts the mechanical power from the turbine into electrical power. The DFIG consists of a three-phase rotor and a three-phase stator. The stator is connected to the wind bus to transmit the electrical power into the grid while the rotor is connected to the B2B converter with associated controllers that control the rotor winding voltage. The stator and rotor are coupled electro-magnetically, which is reflected in the dynamics of the stator and rotor currents expressed in a rotating d-q reference frame [15].

3) *Back-to-Back (B2B) Converter with its Controllers*: The B2B converter is used for regulating the DFIG rotor voltages v_{dr} , v_{qr} as well as the reactive power flowing from the stator to the converter. The B2B converter consists of two three-phase voltage source converters, namely, the rotor-side converter (RSC) and the grid-side converter (GSC), linked via a common DC line [16]. Each of the converters is equipped with a controller. The explanation of the models of GSC, RSC, and their controllers is as follows.

- Following [16], the GSC dynamics is expressed as the variation of the AC-side current in d-q reference frame.

- The GSC controller consists of an inner-loop controller and an outer-loop controller [16]. The objective of the outer-loop controller is to generate a reference signal of the GSC currents i_{dG} , i_{qG} for regulating

TABLE V

NOMENCLATURE FOR THE WIND FARM MODEL. THE SIGNS OF THE CURRENTS ARE POSITIVE WHEN FLOWING IN THE DIRECTION OF THE CORRESPONDING ARROWS IN FIGURE 4. THE VALUES OF THE MODELS PARAMETERS OF A 2MW 690V WIND TURBINE, DFIG ARE SHOWN IN [14], [15]. IN THE FOLLOWING LIST, VALUES RATED AT 100MW, WHICH IS THE SYSTEM CAPACITY USED IN THE SIMULATIONS, ARE SHOWN.

Symbol	Numerical value	Description
Wind turbine		
ω_l, ω_r		angular velocity of low-speed shaft and high-speed shaft
θ_T		torsion angle (rad)
P_a	2.45×10^{-5}	aerodynamic power input depending on wind speed
J_l, J_r	$1.95 \times 10^4, 0.138$	inertia coefficients of the low-speed and high-speed shafts (sec)
B_l, B_r	9.87, 0.001	friction coefficients of the low-speed and high-speed shafts
K_c	508.9	torsional stiffness (1/rad)
d_c	337.76	damping coefficient of turbine
N_g	90	gear ratio
$\bar{\omega}_m$	60π	mechanical synchronous frequency (rad/sec)
DFIG		
i_{dr}, i_{qr}		d- and q-axis rotor currents
i_{ds}, i_{qs}		d- and q-axis stator currents
v_{dr}, v_{qr}		d- and q-axis rotor voltages
T		electromechanical torque converted by DFIG
$P_s + jQ_s$		power flowing from DFIG to bus
γ_w		number of wind generators inside the farm
X_m	197.64	magnetizing reactance
X_{ls}, X_{lr}	4.620, 4.976	stator and rotor leakage reactance
R_s, R_r	0.244, 0.274	stator and rotor resistance
GSC and its controller		
i_{dG}, i_{qG}		d- and q-axis currents flowing from AC side to DC side
m_{dG}, m_{qG}		d- and q-axis duty cycles
$P_r + jQ_r$		power flowing from bus to GSC
Q_r^*	0.001	steady-state value of Q_r
v_{dc}^*	2.03	steady-state DC link voltage
χ_{dG}, χ_{qG}		inner-loop controller state
ζ_{dG}, ζ_{qG}		outer controller state
$i_{dG}^{ref}, i_{qG}^{ref}$		reference signal of i_{dG} and i_{qG}
u_{dG}, u_{qG}		additional control input signals
L_G, R_G	633.46, 0.05	inductance and resistance of GSC
$K_{P,dG}, K_{P,qG}$	0.1, 0.01	P gains of outer controller
$K_{I,dG}, K_{I,qG}$	$1 \times 10^{-4}, 0.001$	I gains of outer controller
τ_G	0.1	GSC current dynamics' time constant to be designed

both of the DC link voltage v_{dc} and the reactive power Q_r flowing into the GSC to their respective setpoints. The outer-loop controller is designed as a PI controller as (20). The inner-loop controller aims at regulating i_{dG}, i_{qG} to the generated reference signals $i_{dG}^{ref}, i_{qG}^{ref}$ by the control of the duty cycles m_{dG}, m_{qG} . Following [16], in this article the controller is designed such that the transfer function from i_{dG}^{ref} (or i_{qG}^{ref}) to i_{dG} (or i_{qG}) is a desired first-order system $1/(\tau_G s + 1)$ when the duty cycles are not saturated. The controller is implemented as (21).

- The RSC model is described as

$$v_{dr} = \frac{L_R}{\bar{\omega}} \dot{i}_{dr} + R_R i_{dr} - L_R i_{qr} + \frac{m_{dR}}{2} v_{dc}, \quad v_{qr} = \frac{L_R}{\bar{\omega}} \dot{i}_{qr} + R_R i_{qr} + L_R i_{dr} + \frac{m_{qR}}{2} v_{dc}, \quad (15)$$

where i_{dr} and i_{qr} are the DFIG rotor currents, m_{dR} and m_{qR} are the duty cycles of the RSC, and v_{dc} is the DC link voltage. In this article, the RSC resistance and inductance are considered to be negligible, that is, $R_R = L_R = 0$. This assumption is always satisfied by incorporating the two into the DFIG rotor circuit. Thus, the RSC model used in this article is described as (22).

- The RSC is equipped with an inner-loop controller and an outer-loop controller. The outer-loop controller generates reference signals for the DFIG rotor currents i_{dr} and i_{qr} for regulating the stator

RSC and its controller		
m_{dR}, m_{qR} χ_{dR}, χ_{qR} $i_{dr}^{ref}, i_{qr}^{ref}$ u_{dR}, u_{qR} $K_{P,dR}, K_{P,qR}$ $\kappa_{P,dR}, \kappa_{P,qR}$ $\kappa_{I,dR}, \kappa_{I,qR}$	0.01, 0.1 5, 5 1, 1	d- and q-axis duty cycles inner-loop controller state reference signal of i_{dr} and i_{qr} additional control input signals P gains of outer controller P gains of the inner-loop controller I gains of the inner-loop controller
DC link		
v_{dc} C_{dc} G_{sw}	448.7 1.2×10^{-5}	DC-side voltage DC link capacitance conductance representing switching loss of the B2B converter
Buck-and-Boost DC/DC converter		
i_{dc} v'_{dc} S	2	current injecting from DC/DC converter into DC link voltage at battery side step down/up gain
Battery		
v_b i'_{dc} C_b G_b R_b, L_b	8.97×10^3 1.2×10^{-5} 0.21, 79.1	battery voltage current injected from the battery battery capacity battery conductance resistance and inductance of battery circuit

voltage magnitude and the high-speed shaft speed ω_r to their setpoints while the inner-loop controller aims at regulating the RSC currents [17]. This control action is actuated through the control of the duty cycles of the B2B converter.

- The RSC and GSC are connected by a DC link equipped with a capacitor whose dynamics is derived from the power balance through the B2B converter [16].

4) *Battery and DC/DC converter*: A battery is used for charging or discharging of electricity whenever needed. The battery comes with a DC/DC converter that steps up/down the battery terminal voltage. Both devices are also sometimes used for suppressing the fluctuations in the output power $P + jQ$ by controlling the DC/DC converter. The model for each is described as follows.

- The DC/DC converter is modeled by buck (step-down) and boost (step-up) models. These models are widely available in the literature [18]. When the converter dynamics are sufficiently fast, simpler models where the output voltage and current are explicit functions of the duty ratio can be derived. In this article this simple model is used.

- The battery circuit is shown as the dark yellow part in Figure 4 [16]. Its dynamics can be represented as the variation of the battery voltage v_b and the output current i'_{dc} .

5) *Interconnection to Grid*: The net active and reactive power injected by the wind farm to the grid are determined as the sum of the power leaving from the stator and that consumed by the B2B converter.

Wind turbine:

$$\begin{cases} J_1 \dot{\omega}_1 = -(d_c + B_1) \omega_1 + \frac{d_c}{N_g} \omega_r - K_c \theta_T + \frac{P_a}{\omega_1}, \\ J_r \dot{\omega}_r = \frac{d_c}{N_g} \omega_1 - \left(\frac{d_c}{N_g^2} + B_r \right) \omega_r + \frac{K_c}{N_g} \theta_T - T, \\ \dot{\theta}_T = \bar{\omega}_m \left(\omega_1 - \frac{1}{N_g} \omega_r \right), \end{cases} \quad (16)$$

where T is defined in (17).

DFIG:

$$\begin{cases} \dot{i} = A_i(\omega_r)i + G_i[\text{Re}(\mathbf{V}), \text{Im}(\mathbf{V})]^\top + B_i[v_{\text{dr}}, v_{\text{qr}}]^\top, \\ T = X_m(i_{\text{ds}}i_{\text{qr}} - i_{\text{qs}}i_{\text{dr}}), \\ P_s + jQ_s = \gamma_W(\text{Re}(\mathbf{V})i_{\text{ds}} + \text{Im}(\mathbf{V})i_{\text{qs}}) + j\gamma_W(\text{Im}(\mathbf{V})i_{\text{ds}} - \text{Re}(\mathbf{V})i_{\text{qs}}), \end{cases} \quad i := \begin{bmatrix} i_{\text{dr}} \\ i_{\text{qr}} \\ i_{\text{ds}} \\ i_{\text{qs}} \end{bmatrix}, \quad (17)$$

where ω_r is defined in (16), v_{dr} and v_{qr} in (22), and

$$A_i(\omega_r) = \frac{1}{\beta} \begin{bmatrix} -R_r X_s & \beta - \omega_r X_s X_r & R_s X_m & -\omega_r X_s X_m \\ -\beta + \omega_r X_s X_r & -R_r X_s & \omega_r X_s X_m & R_s X_m \\ R_r X_m & \omega_r X_r X_m & -R_s X_r & \beta + \omega_r X_m^2 \\ -\omega_r X_r X_m & R_r X_m & -\beta - \omega_r X_m^2 & -R_s X_r \end{bmatrix}, \quad B_i = \frac{1}{\beta} \begin{bmatrix} -X_s & 0 \\ 0 & -X_s \\ X_m & 0 \\ 0 & X_m \end{bmatrix}, \quad (18)$$

$$G_i = \frac{1}{\beta} \begin{bmatrix} X_m & 0 & -X_r & 0 \\ 0 & X_m & 0 & -X_r \end{bmatrix}^\top, \quad X_s := X_m + X_{\text{ls}}, \quad X_r := X_m + X_{\text{lr}}, \quad \beta := X_s X_r - X_m^2.$$

GSC:

$$\begin{cases} \frac{L_G}{\bar{\omega}} \dot{i}_{\text{dG}} = -R_G i_{\text{dG}} + L_G i_{\text{qG}} + \text{Re}(\mathbf{V}) - \frac{m_{\text{dG}}}{2} v_{\text{dc}}, \\ \frac{L_G}{\bar{\omega}} \dot{i}_{\text{qG}} = -R_G i_{\text{qG}} - L_G i_{\text{dG}} + \text{Im}(\mathbf{V}) - \frac{m_{\text{qG}}}{2} v_{\text{dc}}, \\ P_r + jQ_r = \gamma_W(\text{Re}(\mathbf{V})i_{\text{dG}} + \text{Im}(\mathbf{V})i_{\text{qG}}) + j\gamma_W(\text{Im}(\mathbf{V})i_{\text{dG}} - \text{Re}(\mathbf{V})i_{\text{qG}}), \end{cases} \quad (19)$$

where m_{dG} and m_{qG} are defined in (21), and v_{dc} in (25).

Outer-Loop controller of GSC:

$$\begin{cases} \dot{\zeta}_{\text{dG}} = K_{\text{I,dG}}(v_{\text{dc}} - v_{\text{dc}}^*), & \dot{\zeta}_{\text{qG}} = K_{\text{I,qG}}(Q_r - Q_r^*), \\ i_{\text{dG}}^{\text{ref}} = K_{\text{P,dG}}(v_{\text{dc}} - v_{\text{dc}}^*) + \zeta_{\text{dG}}, & i_{\text{qG}}^{\text{ref}} = K_{\text{P,qG}}(Q_r - Q_r^*) + \zeta_{\text{qG}}, \end{cases} \quad (20)$$

where Q_r and v_{dc} are defined in (19) and (25).

Inner-Loop controller of GSC:

$$\begin{cases} \tau_G \dot{\chi}_{\text{dG}} = i_{\text{dG}}^{\text{ref}} - i_{\text{dG}}, \\ m_{\text{dG}} = \text{sat} \left(\frac{2}{v_{\text{dc}}} \left(\text{Re}(\mathbf{V}) + L_G i_{\text{qG}} - R_G \chi_{\text{dG}} - \frac{L_G}{\bar{\omega} \tau_G} (i_{\text{dG}}^{\text{ref}} - i_{\text{dG}}) + u_{\text{dG}} \right) \right), \\ \tau_G \dot{\chi}_{\text{qG}} = i_{\text{qG}}^{\text{ref}} - i_{\text{qG}}, \\ m_{\text{qG}} = \text{sat} \left(\frac{2}{v_{\text{dc}}} \left(\text{Im}(\mathbf{V}) - L_G i_{\text{dG}} - R_G \chi_{\text{qG}} - \frac{L_G}{\bar{\omega} \tau_G} (i_{\text{qG}}^{\text{ref}} - i_{\text{qG}}) + u_{\text{qG}} \right) \right), \end{cases} \quad (21)$$

where i_{dG} and i_{qG} are defined in (19), $i_{\text{dG}}^{\text{ref}}$ and $i_{\text{qG}}^{\text{ref}}$ in (20), v_{dc} in (25), and $\text{sat}(\cdot)$ is a saturation function whose output is restricted within the range of $[-1, 1]$.

RSC:

$$v_{\text{dr}} = \frac{m_{\text{dR}}}{2} v_{\text{dc}}, \quad v_{\text{qr}} = \frac{m_{\text{qR}}}{2} v_{\text{dc}}, \quad (22)$$

where m_{dR} and m_{qR} are defined in (24), and v_{dc} in (25).

Outer-Loop controller of RSC:

$$i_{\text{dr}}^{\text{ref}} = K_{\text{P,dR}}(|\mathbf{V}| - |\mathbf{V}|^*), \quad i_{\text{qr}}^{\text{ref}} = K_{\text{P,qR}}(\omega_r - \omega_r^*), \quad (23)$$

where ω_r is defined in (16).

Inner-Loop controller of RSC:

$$\begin{cases} \dot{\chi}_{dR} = \kappa_{I,dR}(i_{dr} - i_{dr}^{\text{ref}}), \\ m_{dR} = \text{sat} \left(\frac{2}{v_{dc}} \left(\kappa_{P,dR}(i_{dr} - i_{dr}^{\text{ref}}) + \chi_{dR} + u_{dR} \right) \right), \\ \dot{\chi}_{qR} = \kappa_{I,qR}(i_{qr} - i_{qr}^{\text{ref}}), \\ m_{qR} = \text{sat} \left(\frac{2}{v_{dc}} \left(\kappa_{P,qR}(i_{qr} - i_{qr}^{\text{ref}}) + \chi_{qR} + u_{qR} \right) \right), \end{cases} \quad (24)$$

where i_{dr} and i_{qr} are defined in (17), i_{dr}^{ref} and i_{qr}^{ref} in (23), and v_{dc} in (25).

DC link:

$$\frac{C_{dc}}{\omega} \dot{v}_{dc} = \frac{1}{2v_{dc}} \left(\text{Re}(\mathbf{V})i_{dG} + \text{Im}(\mathbf{V})i_{qG} + v_{dr}i_{dr} + v_{qr}i_{qr} - R_G(i_{dG}^2 + i_{qG}^2) \right) - G_{sw}v_{dc} + \frac{1}{2}i_{dc}, \quad (25)$$

where i_{dG} and i_{qG} are defined in (19), v_{dr} and v_{qr} in (22), i_{dr} and i_{qr} in (17), and i_{dc} in (26). When the battery and DC/DC are not connected, $i_{dc} = 0$.

Buck-and-Boost DC/DC Converter:

$$v'_{dc} = p(S + u_S)v_{dc}, \quad i_{dc} = p(S + u_S)i'_{dc}, \quad p(x) = \begin{cases} x & \text{if } x \geq 0, \\ 0 & \text{otherwise,} \end{cases} \quad (26)$$

where v_{dc} and i'_{dc} are defined in (25) and (27).

Battery:

$$\begin{cases} \frac{C_b}{\omega} \dot{v}_b = -i'_{dc} - G_b v_b, \\ \frac{L_b}{\omega} \dot{i}'_{dc} = v_b - R_b i'_{dc} - v'_{dc}, \end{cases} \quad (27)$$

where v'_{dc} is defined in (26).

Interconnection to grid

$$P + jQ = (P_s - P_r) + j(Q_s - Q_r), \quad (28)$$

where P_s and Q_s are defined in (17), and P_r and Q_r in (19).

In reference to (1), the wind farm model with the battery and DC/DC converter can be summarized as:

$$\begin{aligned} x_k &:= [\omega_{1,k}, \omega_{r,k}, \theta_{T,k}, i_k^T, i_{G,k}^T, \chi_{G,k}^T, \zeta_{G,k}^T, \chi_{R,k}^T, v_{dc,k}, v_{b,k}, i'_{dc,k}]^T \in \mathbb{R}^{18}, \\ \zeta_{G,k} &:= [\zeta_{dG,k}, \zeta_{qG,k}]^T, \quad i_{G,k} := [i_{dG,k}, i_{qG,k}]^T, \quad \chi_{\bullet,k} := [\chi_{d\bullet,k}, \chi_{q\bullet,k}]^T, \quad \bullet \in \{G, R\}, \\ u_k &:= [u_{dG,k}, u_{qG,k}, u_{dR,k}, u_{qR,k}, u_{S,k}]^T \in \mathbb{R}^5, \quad \alpha_k := [v_{dc,k}^*, Q_{r,k}^*, |\mathbf{V}_k|^*, \omega_{r,k}^*]^T \in \mathbb{R}^4, \end{aligned} \quad (29)$$

and $f_k(\cdot, \cdot, \cdot; \cdot)$ and $g_k(\cdot, \cdot; \cdot)$ in (1) follow from (16)-(28) for $k \in \mathbb{N}_W$. The steady-state x_k is determined as follows. Note that, given the total generated power $P_k^* + jQ_k^*$, there exists a degree of freedom for determining $P_{r,k}^* + jQ_{r,k}^*$ and $P_{s,k}^* + jQ_{s,k}^*$ satisfying (28) in steady state. Thus, not only the triple $(\mathbf{V}_k^*, P_k^*, Q_k^*)$ but also the pair $(P_{r,k}^*, Q_{r,k}^*)$ needs to be known. In this setting, the pair (x_k^*, α_k) satisfying (3) is uniquely determined.

E. Solar Farms

A solar farm model consists of a PV array, a buck-and-boost DC/DC converter, a DC/AC converter with a controller, and a DC link [19], as shown in Figure 6. The signal-flow diagram for the system is shown in Figure 7. The dynamics of the DC/AC converter, its controller, and DC link are similar to those in the wind farm model, given in (32)-(35). The models of the PV array and DC/DC converter are described as follows.

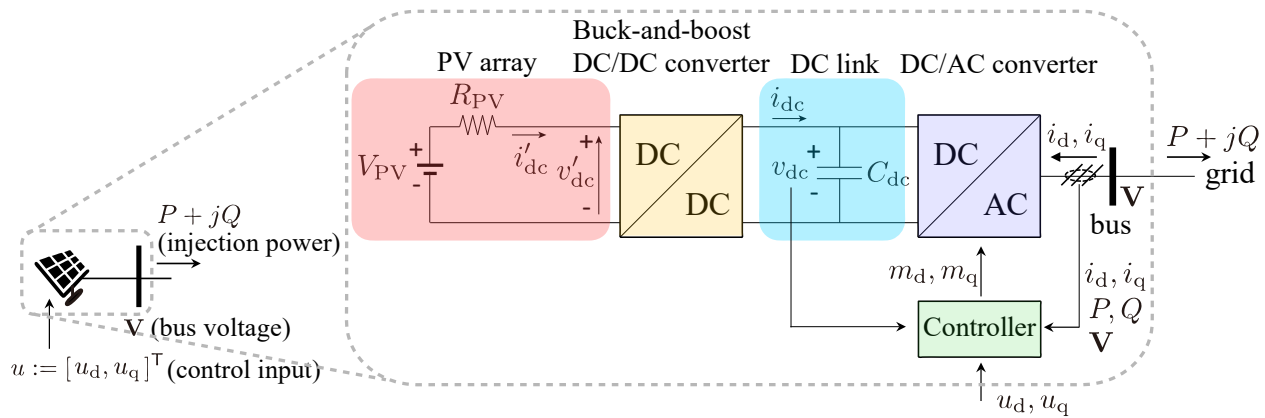


Fig. 6. Equivalent circuit of the model of a solar farm and its terminal bus

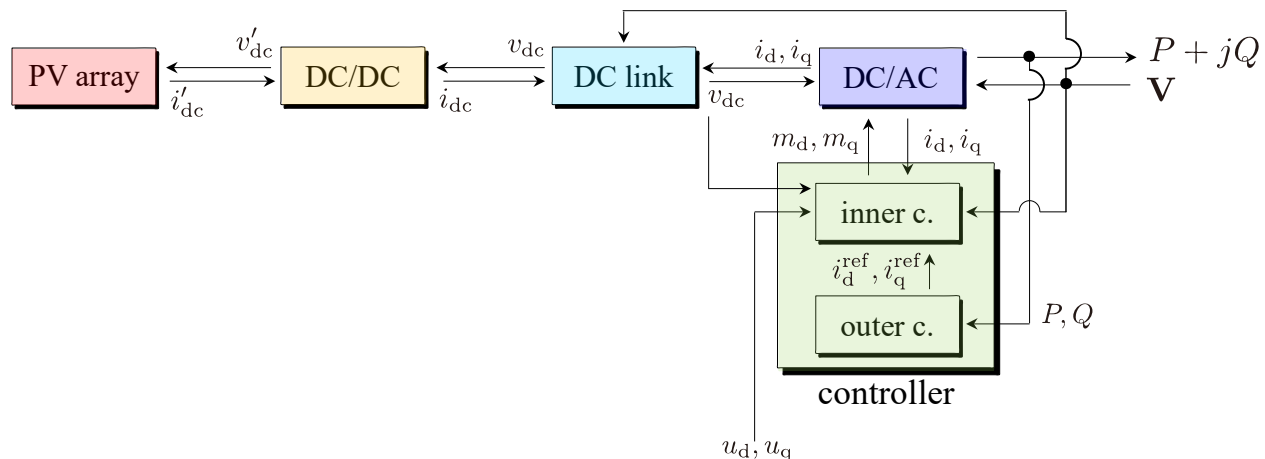


Fig. 7. Signal-flow diagram of the model of a solar farm and its terminal bus, where the constant signal P^* , Q^* , and S are omitted.

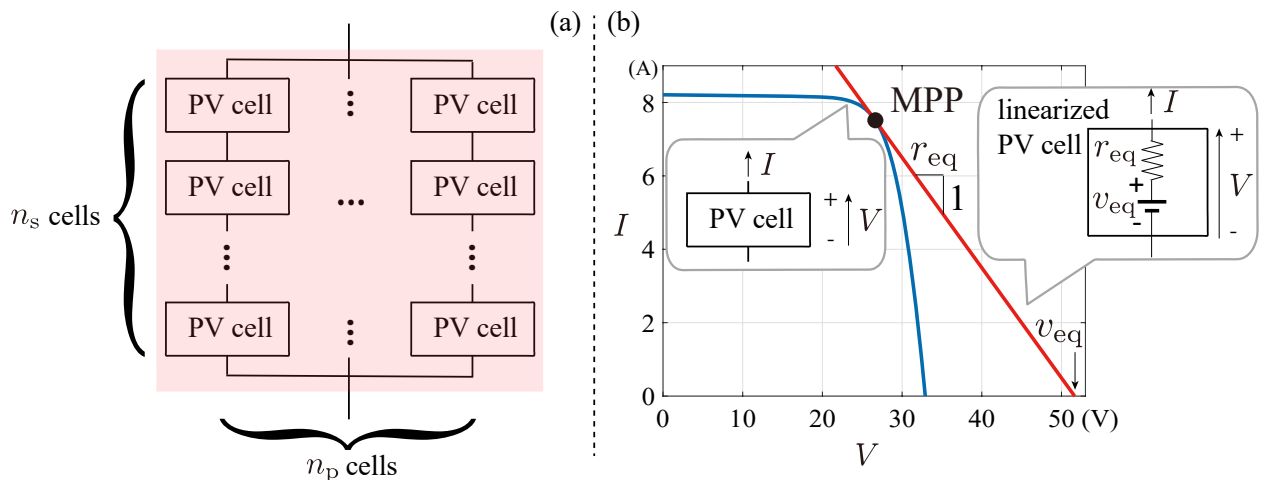


Fig. 8. (a) PV array structure (b) I-V characteristics of PV cell KC200GT

1) *PV array*: The PV array is a parallel interconnection of n_p circuits, each of which contains n_s series-connected PV cells, as shown in Figure 8 (a). Each PV cell is assumed to be identical. Typically, a PV cell has nonlinear I-V characteristics, as shown by the blue line in Figure 8 (b) [19]. Assuming that

TABLE VI

NOMENCLATURE FOR THE SOLAR FARM MODEL. THE SIGNS OF THE CURRENTS ARE POSITIVE WHEN FLOWING IN THE DIRECTION OF THE CORRESPONDING ARROWS IN FIGURE 6. THE VALUES OF THE PV ARRAY PARAMETERS ARE THE CASE WHERE $n_s = 11$ AND $n_p = 1000$ WITH THE KC200GT PV CELL [19]. THE VALUE OF S BELOW IS A TYPICAL ONE BECAUSE THAT WILL CHANGE DEPENDING ON POWER SYSTEM OPERATION CONDITIONS, AS SHOWN IN (37). THE VALUES OF ALL PARAMETERS IN PER UNIT ARE RATED AT 100MW.

Symbol	Numerical value	Description
DC/AC converter and its controller		
i_d, i_q		d- and q-axis currents flowing from AC-side to DC-side
m_d, m_q		d- and q-axis duty cycles
$P + jQ$		power injecting from solar bus
χ_d, χ_q		inner-loop controller state
ζ_d, ζ_q		outer-loop controller state
i_d^{ref}, i_q^{ref}		reference signal of i_d and i_q
u_d, u_q		additional control input signals on duty cycles
γ_{PV}		number of PV generators inside farm
L_{ac}, R_{ac}	39.59, 0.05	inductance and resistance of DC/AC converter
$P^* + jQ^*$	$0.02\gamma_{PV} + j0$	steady-state power injecting from solar bus
$K_{P,d}, K_{I,d}$	-0.01, -0.1	PI gains of d-axis outer-loop controller
$K_{P,q}, K_{I,q}$	0.01, 0.1	PI gains of q-axis outer-loop controller
τ_{ac}	0.7	design parameter representing time constant of converter current dynamics
DC link		
v_{dc}		DC link voltage
C_{dc}	44.87	DC link capacitance
G_{sw}	1.19×10^{-4}	conductance representing switching loss of DC/AC converter
Buck-and-Boost DC/DC converter		
i_{dc}		current flowing from DC/DC converter to DC link
v'_{dc}		voltage at PV array side
S	0.144	step down/up gain so that solar farm is operated at MPP
PV array		
i'_{dc}		current flowing from the PV array to the DC link
R_{PV}	7.687	series resistance inside PV array model
V_{PV}	0.823	voltage of constant voltage source inside PV array

the PV cell is operated around the so-called *maximum power point (MPP)* where the cell output power is maximized, the I-V curve around this point can be approximated by a linear function as shown by the red line. In that case, the PV array can be modeled as a series connection of a constant voltage source with value $V_{PV} := n_s v_{eq}$ and a resistance whose value is $R_{PV} := (n_s/n_p)r_{eq}$. This PV array model is described as (30).

2) *DC/DC converter*: A buck-and-boost DC/DC converter is used to ensure PV cell operation around MPP. This can be done by determining the converter step down/up gain S such that the steady-state PV array output voltage v'_{dc} and current i'_{dc} coincide with the maximum point on the I-V curve. While the gain can be dynamically regulated by controllers, for simplicity, the gain S is supposed to be constant. The DC/DC converter model is described as (31).

PV array:

$$i'_{dc} = \frac{V_{PV} - v'_{dc}}{R_{PV}}, \quad (30)$$

where v'_{dc} is defined in (31).

Buck-and-Boost DC/DC converter:

$$v'_{dc} = S v_{dc}, \quad i_{dc} = S i'_{dc}, \quad (31)$$

where v_{dc} and i'_{dc} are defined in (35) and (30).

DC/AC converter:

$$\begin{cases} \frac{L_{ac}}{\bar{\omega}} \dot{i}_d = -R_{ac}i_d + L_{ac}i_q + \text{Re}(\mathbf{V}) - \frac{m_d}{2}v_{dc}, \\ \frac{L_{ac}}{\bar{\omega}} \dot{i}_q = -R_{ac}i_q - L_{ac}i_d + \text{Im}(\mathbf{V}) - \frac{m_q}{2}v_{dc}, \\ P + jQ = -\gamma_{PV}(\text{Re}(\mathbf{V})i_d + \text{Im}(\mathbf{V})i_q) - j\gamma_{PV}(\text{Im}(\mathbf{V})i_d - \text{Re}(\mathbf{V})i_q), \end{cases} \quad (32)$$

where m_d and m_q are defined in (34), and v_{dc} in (35).

Outer-Loop controller of DC/AC converter:

$$\begin{cases} \dot{\zeta}_d = K_{I,d}(P^* - P), & \dot{\zeta}_q = K_{I,q}(Q^* - Q), \\ i_d^{\text{ref}} = K_{P,d}(P^* - P) + \zeta_d, & i_q^{\text{ref}} = K_{P,q}(Q^* - Q) + \zeta_q, \end{cases} \quad (33)$$

where P and Q are defined in (32).

Inner-Loop controller of DC/AC converter:

$$\begin{cases} \tau_{ac} \dot{\chi}_d = i_d^{\text{ref}} - i_d, \\ m_d = \text{sat} \left(\frac{2}{v_{dc}} \left(\text{Re}(\mathbf{V}) + L_{ac}i_q - R_{ac}\chi_d - \frac{L_{ac}}{\bar{\omega}\tau_{ac}}(i_d^{\text{ref}} - i_d) \right) + u_d \right), \\ \tau_{ac} \dot{\chi}_q = i_q^{\text{ref}} - i_q, \\ m_q = \text{sat} \left(\frac{2}{v_{dc}} \left(\text{Im}(\mathbf{V}) - L_{ac}i_d - R_{ac}\chi_q - \frac{L_{ac}}{\bar{\omega}\tau_{ac}}(i_q^{\text{ref}} - i_q) \right) + u_q \right), \end{cases} \quad (34)$$

where i_d and i_q are defined in (32), i_d^{ref} and i_q^{ref} in (33), and v_{dc} in (35).

DC link:

$$\frac{C_{dc}}{\bar{\omega}} \dot{v}_{dc} = \frac{1}{2v_{dc}} (\text{Re}(\mathbf{V})i_d + \text{Im}(\mathbf{V})i_q + v_{dc}i_{dc} - R_{ac}(i_d^2 + i_q^2)) - G_{sw}v_{dc}, \quad (35)$$

where i_d and i_q are defined in (32), and i_{dc} in (31).

In reference to (1) the solar farm model can be summarized as:

$$\begin{aligned} x_k &:= [i_{d,k}, i_{q,k}, \chi_{d,k}, \chi_{q,k}, \zeta_{d,k}, \zeta_{q,k}, v_{dc,k}]^T \in \mathbb{R}^7, \\ u_k &:= [u_{d,k}, u_{q,k}]^T \in \mathbb{R}^2, \quad \alpha_k := [P_k^*, Q_k^*, S_k]^T \in \mathbb{R}^3, \end{aligned} \quad (36)$$

and $f_k(\cdot, \cdot, \cdot; \cdot)$ and $g_k(\cdot, \cdot; \cdot)$ in (1) follow from (30)-(35) for $k \in \mathbb{N}_S$. The steady-state value of x_k and S_k can be found as follows. Suppose that $(v_{dc,k}^*, i_{dc,k}^*)$ is at the MPP. Given \mathbf{V}_k , P_k , Q_k , $v_{dc,k}^*$ and $i_{dc,k}^*$, the pair (x_k^*, α_k) satisfying (3) are then uniquely determined as $x_k^* = [i_{d,k}^*, i_{q,k}^*, \chi_{d,k}^*, \chi_{q,k}^*, \zeta_{d,k}^*, \zeta_{q,k}^*, v_{dc,k}^*]^T$ and α_k in (36) where

$$\begin{aligned} \begin{bmatrix} \zeta_{d,k}^* \\ \zeta_{q,k}^* \end{bmatrix} &= \begin{bmatrix} \chi_{d,k}^* \\ \chi_{q,k}^* \end{bmatrix} = \begin{bmatrix} i_{d,k}^* \\ i_{q,k}^* \end{bmatrix} = \frac{1}{|\mathbf{V}_k^*|^2} \begin{bmatrix} -\text{Re}(\mathbf{V}_k^*) & -\text{Im}(\mathbf{V}_k^*) \\ -\text{Im}(\mathbf{V}_k^*) & \text{Re}(\mathbf{V}_k^*) \end{bmatrix} \begin{bmatrix} \frac{P_k^*}{\gamma_{PV,k}} \\ \frac{Q_k^*}{\gamma_{PV,k}} \end{bmatrix}, \\ v_{dc,k}^* &= \sqrt{\frac{v_{dc,k}^* i_{dc,k}^* - \left(\frac{P_k^*}{\gamma_{PV,k}} + R_{ac,k}(i_{d,k}^{*2} + i_{q,k}^{*2}) \right)}{2G_{sw,k}}}, \quad S_k = \frac{v_{dc,k}^*}{v_{dc,k}^*}. \end{aligned} \quad (37)$$

F. Energy Storage Systems

The energy storage system consists of a battery, a buck-and-boost DC/DC converter, a DC/AC converter, and a controller, as shown in Figure 9. The basic functions of these four components are to charge/discharge electricity, to step down/up the battery terminal voltage, to rectify the three-phase current to a DC current, and to regulate the DC voltage in between the converters, respectively. When the energy storage system is connected to DC line, the DC/AC converter is not needed. The dynamics of the DC/AC converter, its controller, DC/DC converter, and DC link are similar to those described in equations (32), (33)-(34), (31), and (35), respectively.

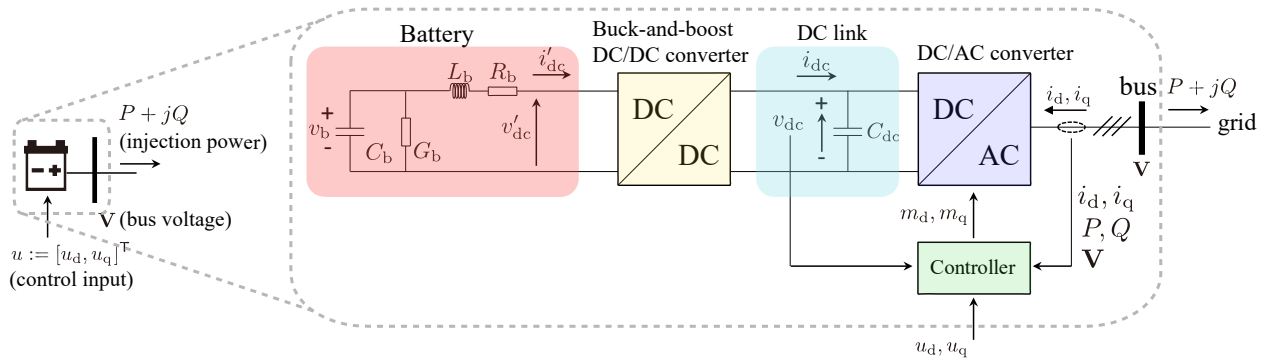


Fig. 9. Physical structure of the model of an energy storage system with its terminal bus

III. IMPACT OF DISTRIBUTED ENERGY RESOURCES ON POWER SYSTEM DYNAMICS AND STABILITY

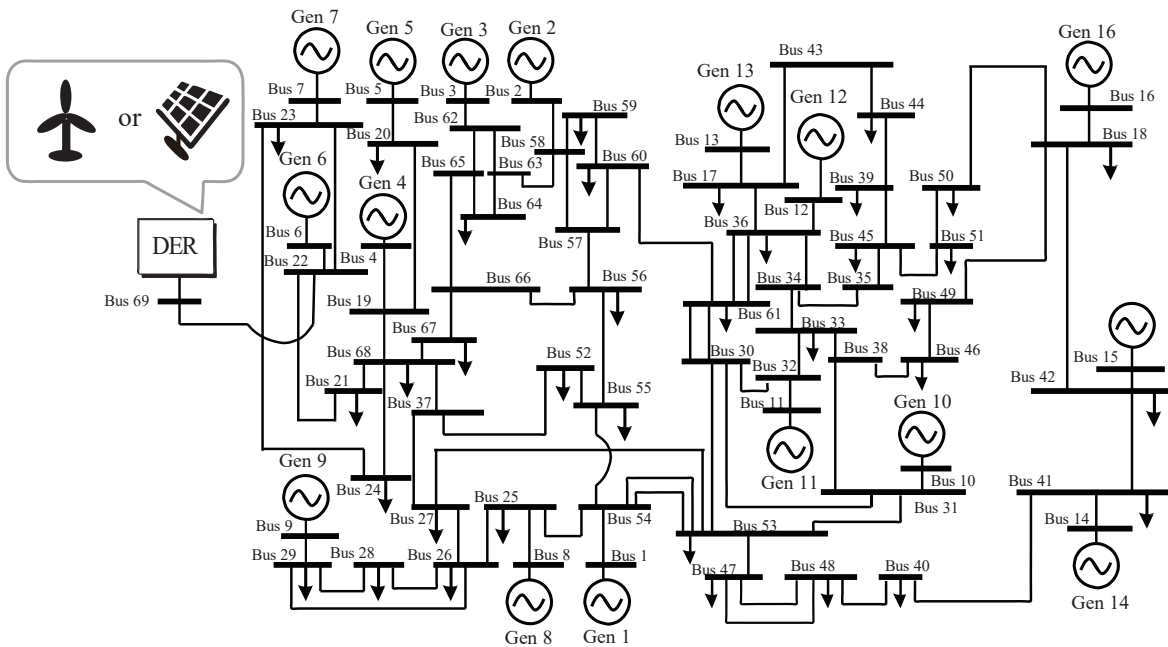


Fig. 10. IEEE 68-bus, 16-machine power system model with one DER. The downward arrows represent load extractions.

Given a DER-integrated power system model (1)-(2), the question is - how does the penetration of DERs and their controllers dictate the stability and dynamic performance of the grid? This section demonstrates these impacts using numerical simulations of the IEEE 68-bus power system model [20]. The MATLAB codes for these simulations can be found in [21]. The network diagram is shown in Figure 10. Each individual component is modeled by the equations listed in the previous section. The DER bus, denoted as Bus 69, connects to Bus 22. The reactance between Bus 22 and 69 represents the transformer for stepping down the grid voltage to the DER voltage. Its value is taken as $j0.01$.

First, consider the DER to be a solar farm as in (30)-(35) with $\mathbb{N}_S = \{69\}$. The other bus indices \mathbb{N}_G , \mathbb{N}_L , \mathbb{N}_N are shown in Figure 10. The model of this PV-integrated power system is the combination of (1)-(2) where Σ_k for $k \in \mathbb{N}_G$, \mathbb{N}_L , \mathbb{N}_N and \mathbb{N}_S are defined as (4)-(8), (12), (11), and (30)-(35). Note that γ_{PV} is the number of PV generators inside the farm. A question here is - how does γ_{PV} affect small-signal stability of the grid? Small-signal stability is defined as the stability of the grid model linearized around its equilibrium [6]. The procedure to obtain the linearized model is as follows: first, compute

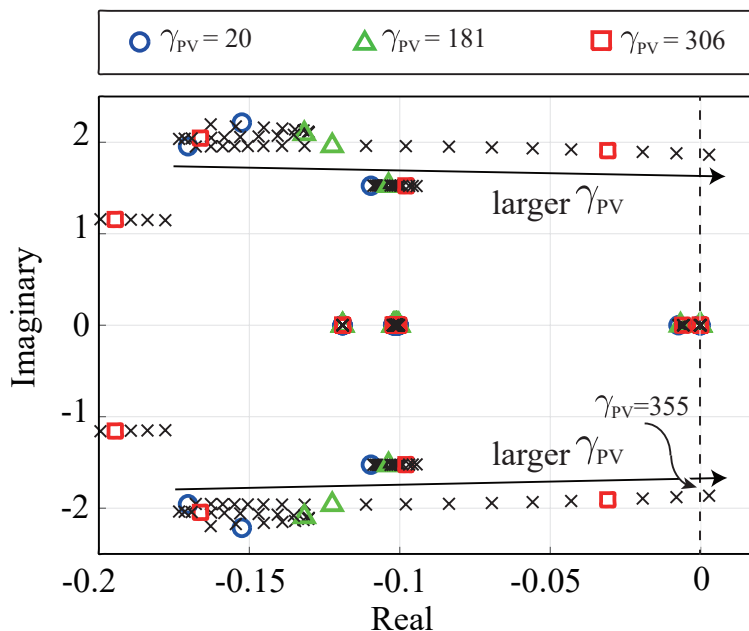


Fig. 11. Variation of 13 dominant eigenvalues of PV-integrated power system.

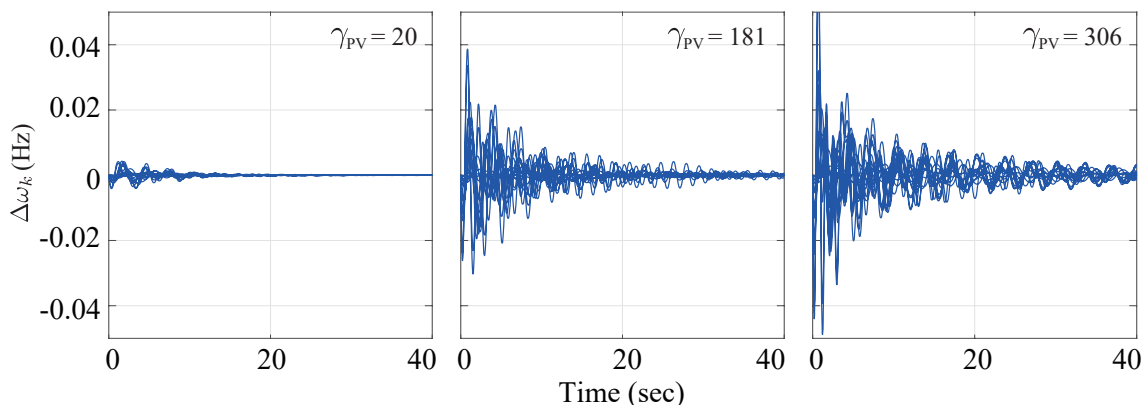


Fig. 12. Trajectories of the frequency deviations of all synchronous generators.

an equilibrium of the entire system (1)-(2), as summarized in the previous section; second, linearize the individual component dynamics (1) and the interconnection equation (2) about this equilibrium. Note that generators, solar farms, and wind farms are dynamical systems while loads, non-unit buses, and the interconnection are static systems. Thus, the d- and q-axis voltages of all buses are redundant states. By eliminating these redundant states from the linearized differential algebraic equation (DAE) model, a linearized ordinary differential equation (ODE) model can be obtained. This method of elimination is referred to as Kron reduction. Figure 11 shows the 13 dominant eigenvalues of this linearized power system model at a desired equilibrium. The eigenvalues around $-0.17 \pm j2$ for $\gamma_{PV} = 20$ start moving to the right as the value of γ_{PV} is increased, and finally cross the imaginary axis when $\gamma_{PV} > 355$, resulting in an unstable system. Each PV generator is rated at 2 MW; therefore $\gamma_{PV} = 355$ means that the net steady-state power output of the solar farm is $P_{69}^* = 710$ MW, which is 3.85% of the total generated power of the system. This may look like a small percentage, but in terms of the stability limit the amount of solar penetration is quite close to critical. This pole shift happens due to the fact that the equilibrium changes with γ_{PV} . When a fault (modeled as an impulse function causing the initial conditions of $i_{d,k}$ and $i_{q,k}$ in (32) to move from their equilibrium values) is induced oscillations in the transient response of the

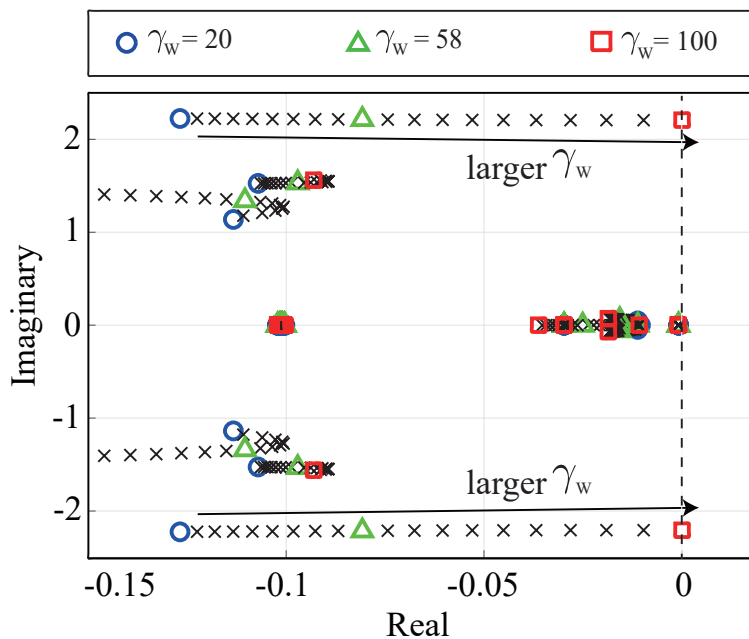


Fig. 13. Variation of 14 dominant eigenvalues of wind-integrated power system.

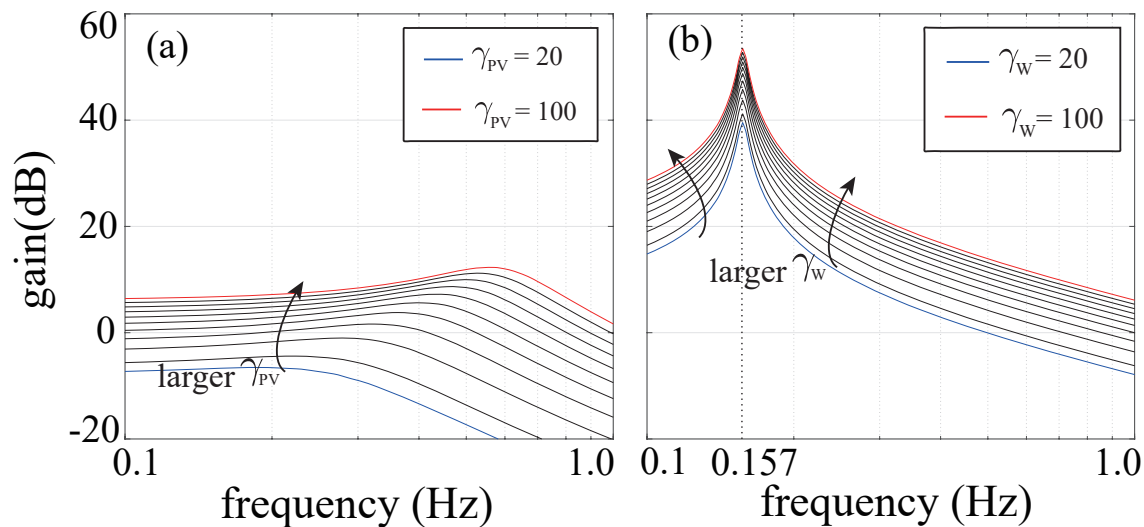


Fig. 14. Singular value plot of the frequency response from $[\text{Re}(\mathbf{V}), \text{Im}(\mathbf{V})]^T$ to $[P, Q]^T$ for the (a) linearized solar farm model, and (b) linearized wind farm model

states can easily be seen. Figure 12 shows the frequency deviation of all 16 synchronous generators for the cases where $\gamma_{PV} = 20, 181, 306$. The results indicate that as γ_{PV} increases the PV-integrated power system, without any DER control, becomes oscillatory with poor damping.

Next, the solar farm at Bus 69 is replaced by a wind farm without a battery or a DC/DC converter. Figure 13 shows the first 14 dominant eigenvalues of the linearized wind-integrated power system at a desired equilibrium. The eigenvalues around $-0.13 \pm 2.1j$ for $\gamma_w = 20$ start moving to the right as the value of γ_w is increased, and finally cross the imaginary axis when $\gamma_w > 100$, resulting in an unstable system. Each wind generator is rated at 2 MW; therefore, $\gamma_w = 100$ means that the net steady-state power output of the farm is $P_{69}^* = 200$ MW. Thus, compared to the PV penetration, the wind penetration in this case poses a greater threat to small-signal stability. To investigate the difference between the two,

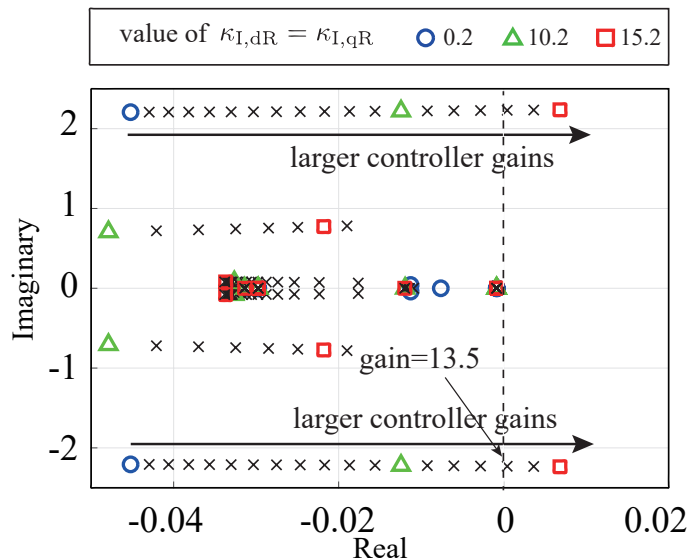


Fig. 15. Variation of ten dominant eigenvalues of wind-integrated power system by changing the integral gains of the RSC controller of the B2B converter

the singular value plot of the frequency response of each model from the d- and q-axis bus voltages $[\text{Re}(\mathbf{V}), \text{Im}(\mathbf{V})]^T$ to the injected power $[P, Q]^T$ is shown in Figure 14 (a) and (b), respectively. The figure shows that the wind farm model has a resonance peak at 0.157 Hz, and the amplitude of the peak increases as γ_w is increased. This is an interesting observation since 0.157 Hz lies in the range of frequencies for the low-frequency (0.1 Hz to 2 Hz) oscillations of the synchronous generators, commonly called inter-area oscillations [22]. The wind injection at Bus 69, thus, stimulates an inter-area mode in this case. The resonance mode actually stems from the internal characteristics of the DFIG dynamic model. Details of this phenomenon can be found in [23]. The PV model, on the other hand, does not show any such resonance peak.

One potential way to combat the poorly damped oscillation would be to tune the PI gains of the converter controller (20)-(21) and (23)-(24). However, such tuning must be done extremely carefully with full knowledge of the entire grid model, since high values of these gains can jeopardize closed-loop stability. This is shown in Figure 15, where the first ten dominant eigenvalues of the linearized closed-loop model for $\gamma_w = 80$ are shown. The integrator gains that are more than 13.5 end up destabilizing the power system. This is because high-gain controllers stimulate the negative coupling effect between the DER and the rest of the grid. These observations show how many of the power system damping controllers used in today's grid can easily become invalid tomorrow. Much more systematic control mechanisms need to be built for the future grid to accommodate deep DER penetration while increasing flexibility and robustness.

IV. NEW APPROACHES FOR CONTROLLING POWER SYSTEMS WITH DISTRIBUTED ENERGY RESOURCES

A. Local Control of Distributed Energy Resources

To counteract the destabilizing effects that may be caused by deep penetration of DERs in a power grid, as shown in the previous section, a local control mechanism for each individual DER needs to be built. A brief survey of local controllers used in today's grid, both with and without DERs, is summarized in Appendix B. One drawback of existing approaches, however, is that although the controller implementation is decentralized, their design is not necessarily so. This means that the controllers are designed jointly based on full knowledge of the entire power system model. As DER penetration is growing at an unpredictably high rate, grid operators must make sure that if more DERs are installed in the future the existing

controllers would not need to be retuned or redesigned from scratch. In other words, the DER controllers to be designed must have *plug-and-play* capability.

A control method called *retrofit control*, recently proposed in [4], [23] can fulfill this objective. Unlike conventional methods listed in Appendix B, this method has an inherent plug-and-play property, and therefore is ideal for local control of DERs. A brief summary of this approach is presented as follows. The dynamical system $\dot{x} = f(x, u)$, where u is input, is said to be stable if the autonomous system under $u = 0$ is asymptotically stable. Consider a power system integrated with solar and wind farms. For $k \in \mathbb{N}_S \cup \mathbb{N}_W$, let the dynamic model of the DER connected to the k -th bus be rewritten as

$$\dot{x}_k = A_k x_k + B_k u_k + \tilde{f}_k(x_k, \mathbf{V}_k, u_k), \quad (38)$$

where

$$A_k := \frac{\partial f_k}{\partial x_k}, \quad B_k := \frac{\partial f_k}{\partial u_k}, \quad \tilde{f}_k(x_k, \mathbf{V}_k, u_k) := f_k(x_k, \mathbf{V}_k, u_k; \alpha_k) - (A_k x_k + B_k u_k),$$

and $f_k(\cdot, \cdot, \cdot; \cdot)$ follows from (30)-(35) for solar farms (when $k \in \mathbb{N}_S$), and from (16)-(28) for wind farms (when $k \in \mathbb{N}_W$). The following assumptions are imposed on the power system.

Assumption 1: The power system model (1)-(2) is stable.

Assumption 2: The DER state vector x_k and its bus voltage \mathbf{V}_k are measurable for each DER.

Assumption 1 can be guaranteed by ensuring that the grid, without any additional controllers, is stable by properly tuning pre-existing controllers such as PSSs. Since PSS guarantees stable operation of all power systems in practice, one can see that this is a fair assumption for a retrofit controller to work in reality.

Assumption 2 is made to simplify the design; the availability of x_k can be relaxed to output feedback case. The goal is to design a decentralized controller for each DER. The two main requirements from this controller are:

- i) The controllers should preserve closed-loop system stability, and also improve the damping of the generator frequency deviations and line flows.
- ii) Each of the controller should depend only on local state feedback from its DER, and not on any states from the rest of the grid including other DERs. The controller should also be designed independent of the model of the rest of the system.

Property (ii) implies that the controllers should be modular by design, and decentralized by implementation.

The input u_k in (38) is considered to be composed of two parts, namely

$$u_k = u_{1,k} + u_{2,k}. \quad (39)$$

The component $u_{1,k}$ is designed under the assumption that $\tilde{f}_k(\cdot, \cdot, \cdot) = 0$ in (38). In other words, the design of $u_{1,k}$ ignores the nonlinearity in (38) including the dependence on \mathbf{V}_k . Note that this assumption is only made to simplify the design of u_k . They do not influence the actual implementation of the control. Then, $u_{1,k}$ in (39) can be simply designed as

$$u_{1,k} = K_k x_k, \quad (40)$$

where K_k makes $A_k + B_k K_k$ Hurwitz. However, in reality this assumption will not be true. Thus, if $u_k = u_{1,k}$ is implemented, then this control will pose serious threat to stability by neglecting the dynamics following from $\tilde{f}_k(x_k, \mathbf{V}_k, u_k)$, and by neglecting the dynamics of the rest of the grid excluding the DER via \mathbf{V}_k , both of which will be stimulated by the control. In order to prevent this stimulation, a compensation signal $u_{2,k}$ is designed for (39) using a dynamic compensator

$$\hat{\Sigma}_k : \begin{cases} \dot{\hat{x}}_k = A_k \hat{x}_k + \tilde{f}_k(x_k, u_k, \mathbf{V}_k) \\ u_{2,k} = -K_k \hat{x}_k, \end{cases} \quad \hat{x}_k(0) = x_k^*. \quad (41)$$

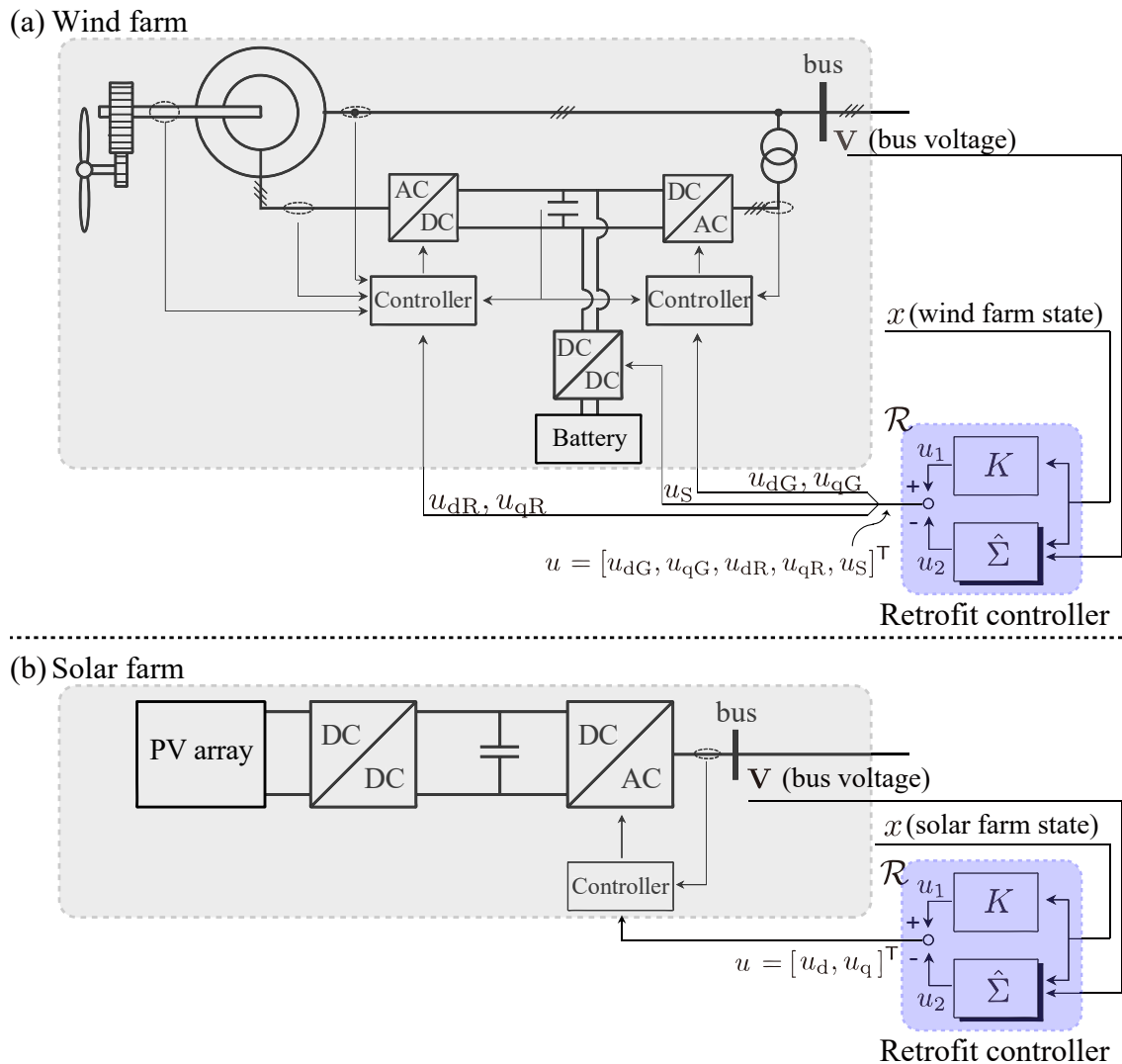


Fig. 16. Signal-flow diagram of DER with the retrofit controller \mathcal{R}_k in (42). Figures (a) and (b) correspond to case where the DER is a wind farm and a solar farm, respectively. In each subfigure, the bus index k is omitted.

The final controller is written as the combination of (39), (40), and (41) as

$$\mathcal{R}_k : \begin{cases} \dot{\hat{x}}_k = A_k \hat{x}_k + \tilde{f}_k(x_k, u_k, \mathbf{V}_k) \\ u_k = K_k x_k - K_k \hat{x}_k, \end{cases} \quad \hat{x}_k(0) = x_k^*. \quad (42)$$

Equation (42) is called a *retrofit controller*. The following proposition holds for this controller.

Proposition 1: Let Assumptions 1 and 2 hold. Then, the interconnection of the power system (1)-(2) and retrofit controllers \mathcal{R}_k in (42) for $k \in \mathbb{N}_S \cup \mathbb{N}_W$ is stable for any K_k such that $A_k + B_k K_k$ is Hurwitz.

The proof of Proposition 1 is shown in [4], [23]. The signal-flow diagram of a DER equipped with the retrofit controller (42) is shown in Figure 16. Proposition 1 shows that the retrofit controllers satisfy the stability requirement in Property (i) listed earlier. Equation (42) shows that the controllers satisfy Property (ii), that is, \mathcal{R}_k can be designed by using information of only $f_k(\cdot, \cdot, \cdot; \cdot)$ and x_k^* of the corresponding DER, which makes it modular; \mathcal{R}_k can be implemented by using feedback from only x_k and \mathbf{V}_k , which makes it decentralized. Neither the model nor the states of the “rest of the grid” are needed for designing or implementing \mathcal{R}_k . The controller gain K_k can be anything as long as $A_k + B_k K_k$ is Hurwitz. For example, given the DER model (38), first design the state-feedback gain as $K_k = -R_k^{-1} B_k^T X_k$ where X_k

is a positive-definite matrix satisfying

$$X_k A_k^\top + A_k X_k - X_k B_k R_k^{-1} B_k^\top X_k + W_k = 0,$$

with suitable weight matrices R_k and W_k , and thereafter design \mathcal{R}_k in (42). This LQR-based retrofit controller will be used in numerical simulations later. Note that the initialization of this controller can also be done in a decentralized manner. The initial state $\hat{x}_k(0)$ is taken as the equilibrium of the DER to be controlled, that is, $\hat{x}_k(0) = x_k^*$, where x_k^* can be computed in advance from the k -th component dynamics under a solution of the power flow calculation. In other words, the initialization of the controller can be done without taking into account any of the other components.

The section is closed by stating two important properties of the retrofit controller.

1. Not just stability, the plug-and-play action of retrofit control can also be used to improve the closed-loop dynamic performance of the grid by proper selection of K_k in (42), which can help in attenuating transient oscillations in the power flows. This will be shown in numerical simulations later. For theoretical details on this point please see [4], [23].

2. Retrofit controllers are most sensitive to faults that occur either at or near the DER bus. This is because closer a fault is to the DER bus, more significant will be the change in the DER initial state from its equilibrium. If, on the other hand, a fault occurs far away from the DER bus so as to cause practically no change in its initial state, then the retrofit controller will show no effect. This property implies that retrofit controllers can be added to or removed from the grid in a plug-and-play fashion without creating any sensitivity to other retrofit controllers. This modularity property of retrofitting will be illustrated shortly by numerical simulations of the IEEE 68-bus system. For more theoretical details on this point, please see [23].

B. Wide-Area Control

Retrofit control is ideal for handling local disturbances. A separate layer of control is needed for handling disturbances that cause system-wide impacts on the entire grid. These controllers are called wide-area controllers. They are commonly actuated through additional control loops in the PSSs of synchronous generators. Ideally speaking, one can consider using retrofit control for designing wide-area controllers as well. However, the assets in the legacy grid excluding DERs do not fluctuate much over longer terms, and therefore do not necessarily need a plug-and-play type modular control in excess of what is already provided by the conventional PSS. Thus, in practice, retrofitting may be an overkill for WAC. A typical WAC problem is formulated as follows. Consider a power system consisting of generators, loads, non-unit buses, wind/solar farms. The entire system dynamics is described as (1) and (2). The variables $P_k + jQ_k$ and \mathbf{V}_k for $k \in \{1, \dots, N\}$ are *auxiliary* variables which can be eliminated to convert the differential-algebraic model into an ordinary differential equation model by a process called Kron reduction [6]. By linearizing the Kron-reduced model about a desired equilibrium, the model of the power system is written in a compact form as

$$\dot{\tilde{x}}_G = A_G \tilde{x}_G + B_G u_G + R_G \tilde{x}_D, \quad \dot{\tilde{x}}_D = A_D \tilde{x}_D + B_D u_D + R_D \tilde{x}_G, \quad (43)$$

where $\tilde{x}_G \in \mathbb{R}^{7|\mathbb{N}_G|}$ and $\tilde{x}_D \in \mathbb{R}^{7|\mathbb{N}_S|+18|\mathbb{N}_W|}$ are the stacked representations of the generator state error and the DER state error relative to the equilibrium x_k^* for $k \in \mathbb{N}_G$ and $k \in \mathbb{N}_S \cup \mathbb{N}_W$, respectively, and $u_G \in \mathbb{R}^{|\mathbb{N}_G|}$ and $u_D \in \mathbb{R}^{|\mathbb{N}_S|+|\mathbb{N}_W|}$ are the stacked representations of u_k for $k \in \mathbb{N}_G$ and $k \in \mathbb{N}_S \cup \mathbb{N}_W$, respectively. The k -th element of u_G represents a signal actuated through the PSS, as explained in (6). Ideally speaking, both u_G and u_D should be used for WAC. However, since in the current state-of-art the penetration of DERs in most power systems is still quite small most wide-area controller design are based on the generator models only, ignoring the dynamics of the DERs. In other words, consider a model of the form

$$\dot{\xi}_G = A_G \xi_G + B_G u_G, \quad \xi(0) = \tilde{x}_G(0). \quad (44)$$

A WAC problem for POD can then be defined as finding a gain matrix K_G such that

$$u_G = K_G \xi_G, \quad K_G \in \mathcal{S}, \quad (45)$$

minimizes

$$J := \int_0^\infty (\xi_G^\top(t) Q \xi_G(t) + u_G^\top(t) R u_G(t)) dt, \quad (46)$$

for a given positive-semidefinite matrix Q and a positive-definite matrix R , subject to (44). In (45), $\mathcal{S} \subseteq \mathbb{R}^{|\mathbb{N}_G| \times 7|\mathbb{N}_G|}$ represents admissible controllers encapsulating the distributed nature of the controller. Alternative formulations have also been proposed, an overview of which is summarized in Appendix C. Once K_G is designed, the wide-area control is implemented as $u_G = K_G \tilde{x}_G$ in (43) by setting up a sparse communication network between the designated set of generators. For simplicity, the communication is assumed to be ideal, that is, it does not have any delays or packet losses. Works on WAC under communication delays or packet losses can be found in papers such as [24], [25]. The generator state vector \tilde{x}_G is assumed to be available (for state estimation of \tilde{x}_G using PMU measurements and decentralized Kalman filters, please see [2], [26], [27], [28], [29]). Owing to the wide availability of PMU data, utilities these days have reasonably good models for their operating regions. The independent system operators also have fairly accurate power system models. For a robust implementation of WAC these models should be updated every few hours using fresh PMU data as the operating point changes, followed by an update in K_G .

The goal of the constraint in (45) is to promote sparsity in K_G for minimizing the density of the underlying communication network without sacrificing closed-loop performance much. The usual philosophy for constructing \mathcal{S} is as follows. For a natural number $L \leq |\mathbb{N}_G|$, consider a set of groups $\{\mathcal{G}_l\}_{l \in \{1, \dots, L\}}$ such that $\bigcup_{l \in \{1, \dots, L\}} \mathcal{G}_l = \{1, \dots, |\mathbb{N}_G|\}$. Note that the groups are not necessarily disjoint, namely, there may exist pair (l, l') such that $\mathcal{G}_l \cap \mathcal{G}_{l'} \neq \emptyset$. Let $K_{G,ij} \in \mathbb{R}^{1 \times 7}$ denote the (i, j) -block matrix of K_G . Define \mathcal{S} as

$$\mathcal{S} := \{K_G : K_{G,ij} = 0, \text{ there does not exist } l \in \{1, \dots, L\}, \text{ s.t. } i \in \mathcal{G}_l \wedge j \in \mathcal{G}_l\}. \quad (47)$$

The problem then is to find K_G in (45) minimizing (46) under the constraint \mathcal{S} as in (47). The (sub)optimal set of groups $\{\mathcal{G}_l\}_{l \in \{1, \dots, L\}}$ and the structured feedback gain K_G can be constructed in different ways depending on the objective of the controller. For POD problems operators are often interested in damping only the inter-area oscillation modes. In that case, \mathcal{G}_l can be chosen in the following way, as recently shown in [5]. Modeling the fault as an impulse input, let the small-signal impulse response of any generator frequency deviation be written as

$$\Delta \tilde{\omega}_i(t) = \underbrace{\sum_{j=1}^{\kappa} (\alpha_{ij} \exp(\lambda_j t) + \alpha_{ij}^* \exp(\lambda_j^* t))}_{\text{inter-area modes}} + \underbrace{\sum_{i=\kappa+1}^n (\beta_{ij} \exp(\rho_j t) + \beta_{ij}^* \exp(\rho_j^* t))}_{\text{other modes}}, \quad (48)$$

where κ is the number of local modes (explained later), n is the dimension of the entire system, $\alpha_{ij}, \lambda_i, \beta_{ij}, \rho_i$ are modal coefficients, and $*$ is the complex conjugate operator. Assuming that the other modes are sufficiently damped by PSSs as a result of which their effect dies down quickly, the goal is to add damping to only the inter-area oscillation modes. The dominance of the inter-area modes is defined based on the magnitude of the modal coefficients α_{ij} . For example, consider a power system including four generators (namely $|\mathbb{N}_G| = 4$), with three inter-area modes (namely $\kappa = 3$). Let the residues $\alpha_{11}, \alpha_{21}, \alpha_{31}, \alpha_{32}, \alpha_{42}$ be classified as dominant residues because they satisfy $|\alpha_{ii}| \geq \mu$, where μ is a pre-specified threshold. In other words, it is assumed that the inter-area modes λ_1, λ_2 are substantially excited by the incoming disturbance while the third inter-area mode has much poorer participation in the states. From the indices of the dominant modes, one can construct the two sets

$$\mathcal{G}_1 = \{1, 2, 3\}, \quad \mathcal{G}_2 = \{3, 4\}, \quad (49)$$

indicating that the generators in the first group participate dominantly in λ_1 , and those in the second group participate dominantly in λ_2 . This grouping information is then used to decide the topology of communication. In general, the rule is that the generators inside the l -th group should communicate with each other for suppressing the amplitude of oscillations excited by the mode λ_l . The mode λ_3 for the above example is poorly excited, and therefore, is ignored in the control design. The structure of K_G for this 4-machine example is then constructed as (45) with the structure constraint (47) defined by the group set (49). For this example, the controllers can be written as

$$\begin{aligned}\mathcal{K}_1 : u_1 &= K_{G,11}\tilde{x}_1 + K_{G,12}\tilde{x}_2 + K_{G,13}\tilde{x}_3, \\ \mathcal{K}_2 : u_2 &= K_{G,21}\tilde{x}_1 + K_{G,22}\tilde{x}_2 + K_{G,23}\tilde{x}_3, \\ \mathcal{K}_3 : u_3 &= K_{G,31}\tilde{x}_1 + K_{G,32}\tilde{x}_2 + K_{G,33}\tilde{x}_3 + K_{G,34}\tilde{x}_4, \\ \mathcal{K}_4 : u_4 &= K_{G,43}\tilde{x}_3 + K_{G,44}\tilde{x}_4.\end{aligned}$$

Due to the sparse structure of the communication network, the controllers are implemented in a distributed way as opposed to all-to-all communication that would be equivalent to centralized implementation. Finally, the non-zero entries of K_G are computed by using sub-optimal structured LQR algorithms such as L_1 -sparse optimal control via ADMM [30].

C. Combined Control Architecture for Tomorrow's Grids

The relative advantage between retrofit control and WAC lies in their effectiveness towards different types of faults and the fault locations. Retrofit control of DERs, for example, is more effective than WAC when a fault changing the DER initial state from its equilibrium occurs either at or closer to the DER bus. This is because the former has a high controllability on the DER states, while the latter, being actuated through the AVR and PSS of synchronous generators, has much lower controllability on the DER states. Similarly, WAC is much more effective than retrofit control when a fault happens at non-DER buses. Thus, to accommodate all types of fault scenarios the control architecture for future grids must be a combination of two layers - first, a completely decentralized retrofit control mechanism for each individual DER, and second, a distributed, peer-to-peer communication based wide-area control between the synchronous generators. The modularity of retrofit controllers will enable smoother integration of renewables into the grid in a plug-and-play fashion without jeopardizing stability, or without having to retune the existing PSS gains. WAC, on the other hand, will be necessary to balance out the increasing dynamic interdependence of grid components that may be geographically distant but are electrically close due to more transmission lines being built. The combination of these two control layers is shown in the form of an architectural diagram in Figure 17.

V. NUMERICAL SIMULATIONS

This section demonstrates the effectiveness of the combined retrofit and wide-area control through simulation of the IEEE 68-bus power system model with DERs. The Matlab codes for all of these simulations have been made public at the repository [21]. First, let a single wind farm be connected to Bus 69, as shown in Figure 10, and the effectiveness of the retrofit control is investigated. Let $\gamma_W = 60$. The behavior of this wind-integrated power system after a fault, modeled as an impulsive change in the angular velocity of the low-speed shaft of the wind turbine, is simulated. Let $\omega_1(0) = 0.3\omega_1^*$. In Figures 18(a)-(e), the red lines show the trajectories of the DFIG rotor speed ω_r in (16), the DFIG stator currents i_{ds} and i_{qs} in (17), the active and reactive power P and Q in (28) injected by the wind farm, the GSC duty cycles m_{dG} and m_{qG} in (21), and the frequency deviation $\Delta\omega$ in (4) of all synchronous generators. The fault causes a decrement in the rotor speed ω_r , and induces oscillations in the DFIG stator currents because of the resonance phenomenon described earlier. Both active power P and reactive power Q injected to the grid from the wind farm start oscillating, which in turn induces oscillations in the generator frequencies.

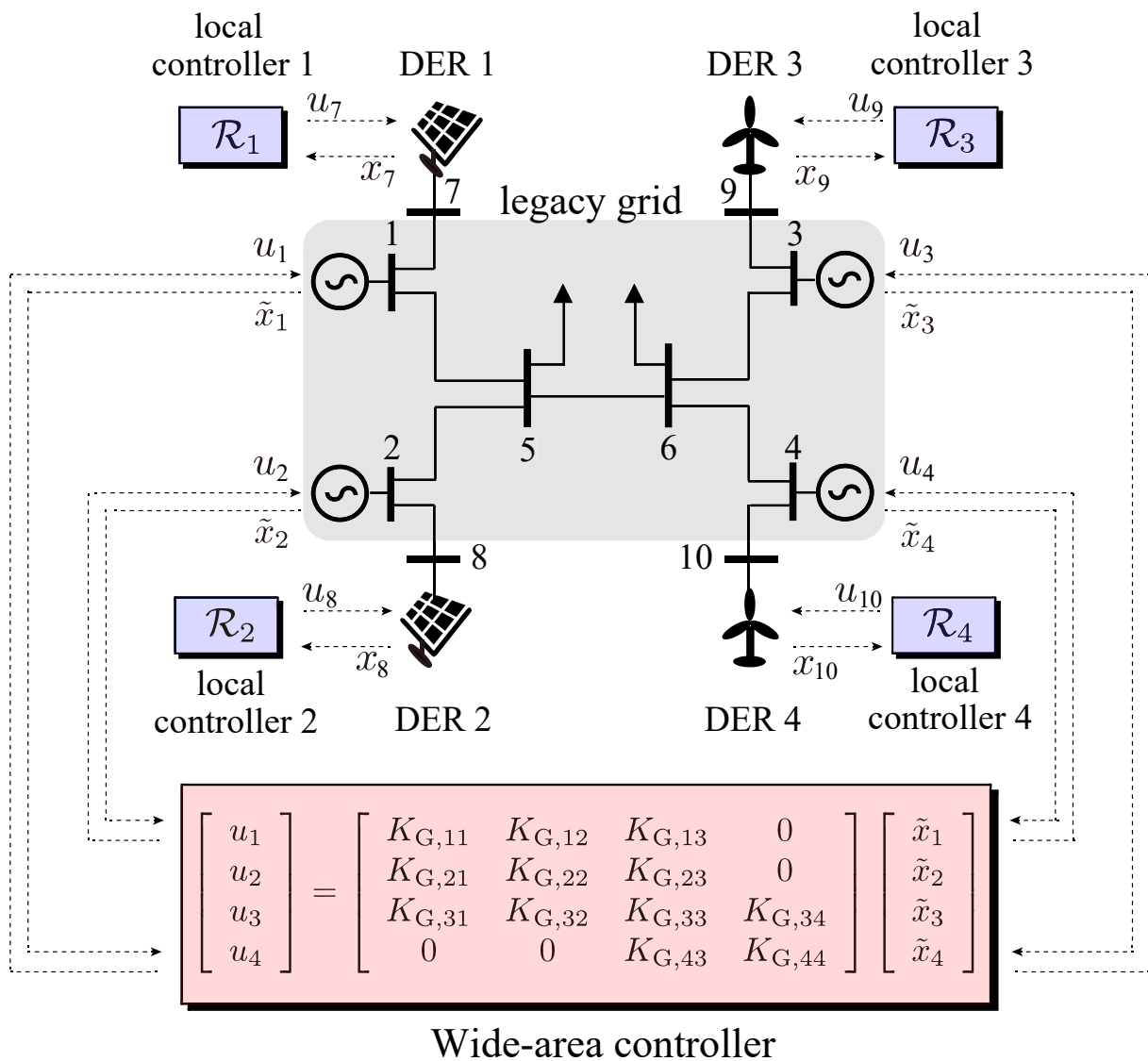


Fig. 17. Grid control architecture showing the co-existence of local and wide-area controllers for a 4-machine power system with four DERs. The local controller \mathcal{R}_k is designed in (42). The wide-area controller K_G in (45) is designed for the two groups $\mathcal{G}_1 = \{1, 2, 3\}$ and $\mathcal{G}_2 = \{3, 4\}$. The sparse structure of WAC avoids the need for all-to-all communication between the generators.

Thus, although the grid is small-signal stable the impact caused by the fault makes the system leave its domain of attraction, resulting in transient instability.

The retrofit controller (42) is next used to counteract this instability. Since the instability is caused by the oscillations of the DFIG currents the state feedback gain K_k is designed to attenuate these oscillations using a LQR controller. In Figures 18(a)-(e), the blue lines show the trajectories of ω_r , i_{ds} and i_{qs} , P and Q , m_{dG} and m_{qG} , and $\Delta\omega$ of the closed-loop system, respectively. By comparing the red lines and blue lines in Figures 18(b)-(c), it can be seen that the oscillations in the stator current and the output power are significantly mitigated by retrofit control. As a result, as shown in Figure 18(e), the oscillations in the frequency deviations are also reduced. However, the oscillations reappear after $t > 150$ sec as the duty cycles m_{dG} and m_{qG} of the GSC in (21) become saturated after this time. This is shown in Figure 18(d). Since the duty cycles are inversely proportional to v_{dc} , this saturation tends to occur when the DC link voltage is small. Furthermore, as shown in Figures 18(a) and (c), there exist negative offsets in ω_r and P . This implies that some of the mechanical power and output wind power are less than their desired values due to the decrement of the low-speed shaft speed.

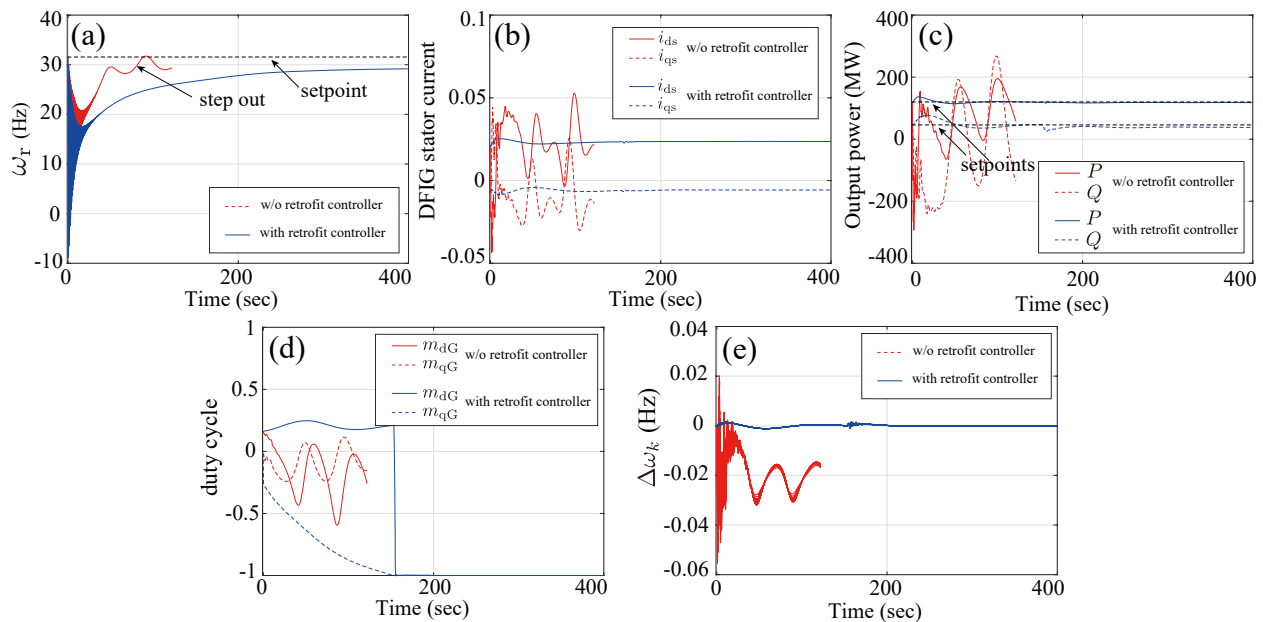


Fig. 18. (a) Trajectories of the DFIG rotor speed, (b) the DFIG stator currents, (c) the active and reactive power injected from the wind farm, (d) the GSC duty cycles, and (e) the frequency deviation of all synchronous generators.

Both of these shortcomings can be resolved by adding a battery to the DC link. The battery can compensate for the DC-link voltage variation, and can discharge energy to make up for the insufficient power. Figure 19(f) shows that the battery voltage reduces as the battery discharges stored energy. Comparing the blue lines in Figures 18(a) and (c) with those in Figures 19(a) and (c), it can be seen that the rotor speed and the injected wind power now both converge to their respective setpoints. Furthermore, the duty cycles are no longer saturated as the DC-link voltage remains almost constant. The battery voltage converges to its setpoint value asymptotically.

Over time new DERs will be added to the existing grid. To emulate this, next, a solar farm with its bus (denoted Bus 70) is added at Bus 66, as shown in Figure 20. The system behavior is investigated after installing the second retrofit controller at this solar farm while retaining the first one at the wind farm. The design of the second retrofit controller follows the same procedure as the first. Figure 21 shows the trajectories of all generator frequency deviations when a fault happens at the solar farm (Fault 1). Figure 21(b) shows the control input calculated by the first and second retrofit controller. It can be seen that the first retrofit controller is inactive in this situation, meaning that it does not have any influence on the closed-loop response. The second retrofit controller, on the other hand, improves damping as soon as it is activated, as depicted by the blue solid lines in Figure 21(a). This shows that retrofit controllers can be added to or removed from the grid in a plug-and-play fashion without creating any sensitivity to other retrofit controllers. The design enjoys a natural decoupling property from one DER to another.

When the fault happens at the DER bus then the retrofit controller alone is sufficient for mitigating oscillations. Any additional wide-area control action may not be necessary in that situation. To show this fact, a LQR-based wide-area controller is designed for all the 16 synchronous generators, and actuated through their PSSs following the fault at the wind farm (Fault 2). Figures 22a summarizes the different ways in which the power system reacts to this fault. Since the fault occurred at the DER bus, the retrofit controller at the DER in Case 2 successfully cancels its adverse effect, and mitigates the oscillations in both the generators and the DER, as shown in (a21) and (a22). If only WAC is used in this situation without any retrofit at the DER, which is Case 3 in the figure, then an interesting observation is made: the generators are damped well, but the DER response is still unacceptably oscillatory. This clearly shows that WAC has limited controllability on the DER states, and thus for this situation using only WAC is not

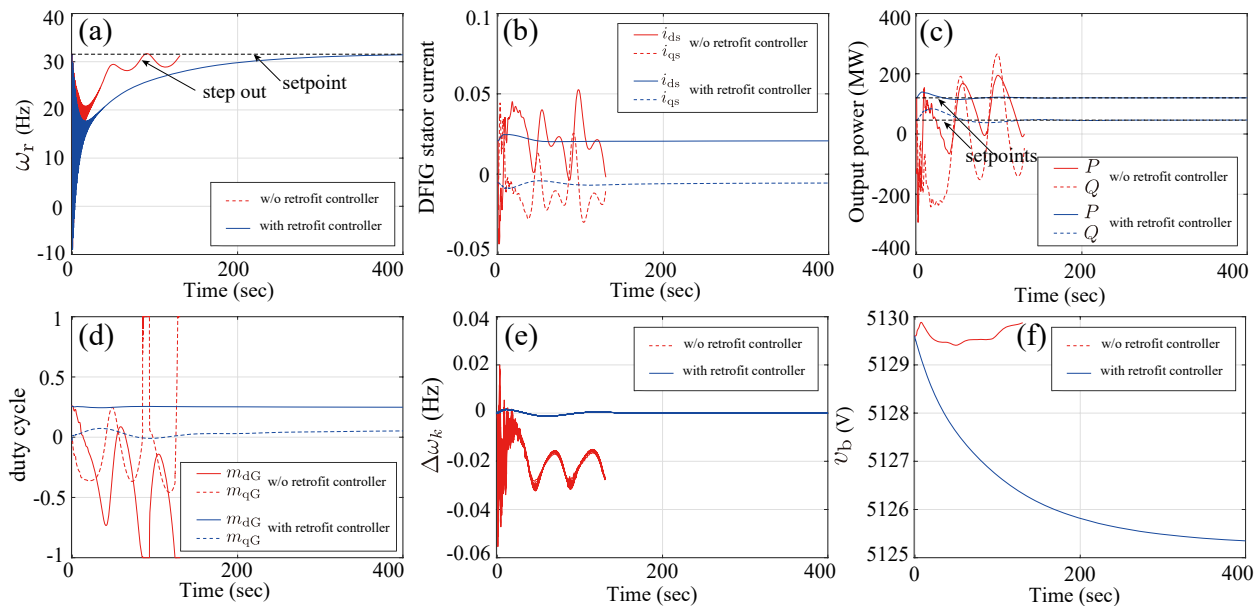


Fig. 19. (a) Trajectories of the DFIG rotor speed, (b) the DFIG stator currents, (c) the active and reactive power injected from the wind farm, (d) the GSC duty cycles, (e) the frequency deviation of all synchronous generators, and (f) battery voltage.

going to suppress all oscillations. Retrofit control is absolutely imperative for this case. The respective responses are shown in (a31) and (a32). However, when the fault happens outside the wind farm, then the retrofit controller is completely inactive and the wide-area controller becomes necessary. To show this, a three-phase fault is induced at Bus 10 (Fault 3) with the fault clearing time 0.07 (sec). By comparing the subfigures (b11)-(b33), it can be seen that the retrofit controllers at the wind and solar farms are no longer effective whereas the wide-area controller successfully damps the power flow oscillations.

Finally, Figures 22(a41)-(a42) and (b41)-(b42) show the case when the two retrofit controllers and the wide-area controller are all used together in the system. The combination can now handle faults occurring at both DER buses and non-DER buses. The simulations bear a clear message that future power grids must have both control architectures implemented on top of each other to enjoy their combined benefits.

VI. CONCLUSION AND FUTURE WORKS

With proliferation of distributed renewable generation many interesting opportunities for control and optimization are arising in power system research. On one hand, wide-area control is becoming essential to make the grid more resilient against blackouts, while on the other hand local plug-and-play type controllers are becoming essential for renewable energy sources. This article proposed a control architecture that combines these two types of controllers, highlighting various design and implementation challenges and solutions for both. The vision here is that this architecture will serve as a platform for control theorists and power engineers to work together, and create a sustainable and secure future for electric energy supply in every corner of the world. A list of open questions is presented for future work.

1. Not only the level of penetration of DERs, but also their relative locations in the grid may have a significant influence on power system stability. For example, with reference to the simulation example presented in the article, when a wind farm with output power 200MW is connected to Bus 22 of the IEEE 68-bus model, the power system model becomes unstable. But, instead, if a wind farm with output power 58MW is connected to Bus 42, the system becomes unstable. More work is needed to understand the system-level characteristics of power system models that decide how the spatial distribution of DERs may or may not preserve stability.

2. The controllers outlined in this article are meant to address transient stability and damping performance. In an actual grid, however, many other parallel control mechanisms will also exist - for

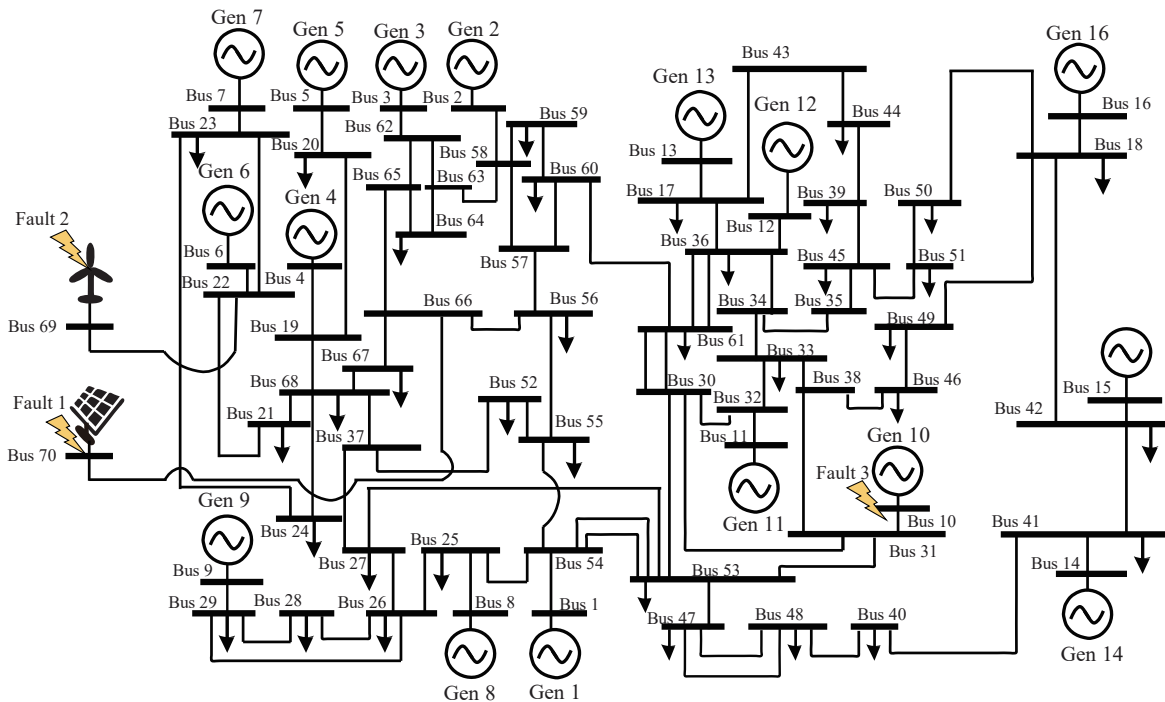


Fig. 20. IEEE 68-bus, 16-machine power system model with two DERs. A single wind farm (with Bus 69) is added to Bus 22 while a single solar farm (with Bus 70) is added to Bus 66.

example, load frequency control (LFC) which maintains the grid frequency at the synchronous value despite fluctuations in loads. Typically, LFC is designed independent of WAC and DER control because of its slower time-scale. However, with gradual disintegration of the grid into smaller micro-grids this time-scale separation may become less dominant leading to a stronger coupling between the controllers. The positive and negative effects of this coupling needs more research.

3. Many open challenges exist for wide-area control as well. For example, instead of updating A_G and B_G in (43) with new PMU data every few hours and redesigning K_G in (45), a future option can be to learn K_G directly after a contingency using online reinforcement learning, Q-learning, adaptive dynamic programming, and similar model-free learning methods. This online learning approach, in fact, will become important if the contingency changes the nominal A_G and B_G significantly. Furthermore, both u_G and u_D in (43) must be used for WAC design in the future grid to accommodate the coupling effects between \tilde{x}_G and \tilde{x}_D . Some recent paper such as [31] have reported preliminary results along these lines where wind power controllers have been used in conjunction to conventional PSS controllers for taking wide-area damping control action. Much more work, however, is needed on this topic, especially with regards to the time-scale separation between u_G and u_D , and also on the sensitivity between the retrofit and WAC parts of u_D .

All of these questions deserve dedicated attention from researchers with backgrounds in control theory, power systems, signal processing, economics, and machine learning.

VII. ACKNOWLEDGEMENTS

This research was supported by CREST, JST Grant Number JPMJCR15K1, Japan. The work of the second author was partly supported by the US National Science Foundation under grant ECCS 1711004. The authors would like to thank the fourth author's secretary Akiho Setoguchi for her help with drawing several illustrations used throughout the paper.

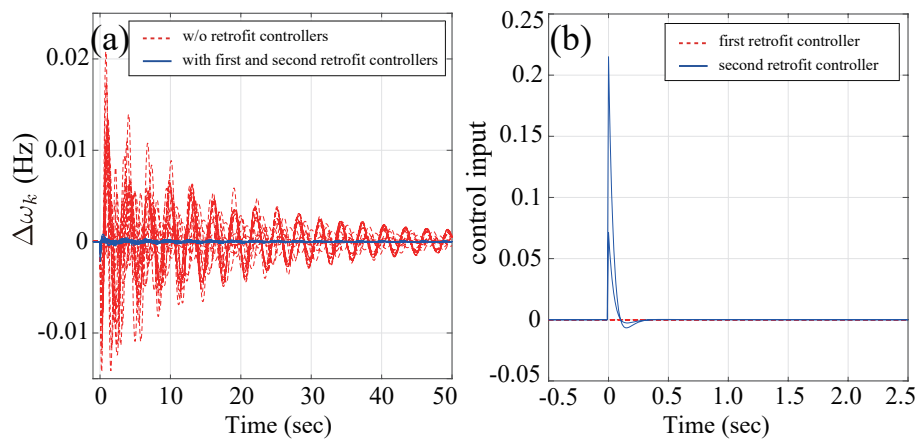


Fig. 21. (a) Trajectories of the frequency deviation of all synchronous generators. The first and second retrofit controllers are implemented to the wind and solar farms at Bus 69 and 70, respectively. (b) Trajectory of the control input u_k generated by the first and second retrofit controllers when Fault 1 happens.

REFERENCES

- [1] U.S. Department of Energy, “Strengthening america’s energy security with offshore wind,” *Technical report*, 2012, available at: <https://www.nrel.gov/docs/fy12osti/49222.pdf>.
- [2] B. Fardanesh, S. Zelingher, A. S. Meliopoulos, G. Cokkinides, and J. Ingleson, “Multifunctional synchronized measurement network,” *IEEE Computer Applications in Power*, vol. 11, no. 1, pp. 26–30, 1998.
- [3] A. Chakraborty and P. P. Khargonekar, “Introduction to wide-area control of power systems,” in *Proc. of American Control Conference*, 2013, pp. 6758–6770.
- [4] T. Ishizaki, T. Sadamoto, J. Imura, H. Sandberg, and K. H. Johansson, “Retrofit control: Localization of controller design and implementation,” *Automatica*, vol. 95, pp. 336–346, 2018.
- [5] A. Jain, A. Chakraborty, and E. Biyik, “An online structurally constrained lqr design for damping oscillations in power system networks,” in *Proc. of American Control Conference*, 2017, pp. 2093–2098.
- [6] P. Kundur, *Power system stability and control*. McGraw-Hill Education, 1994.
- [7] B. Pal and B. Chaudhuri, *Robust control in power systems*. Springer Science & Business Media, 2006.
- [8] W. Dib, R. Ortega, A. Barabanov, and F. Lamnabhi-Lagarrigue, “A ”globally” convergent controller for multi-machine power systems using structure-preserving models,” *IEEE Transactions on Automatic Control*, vol. 54, no. 9, pp. 2179–2185, 2009.
- [9] N. Tsofas, A. Arapostathis, and P. Varaiya, “A structure preserving energy function for power system transient stability analysis,” *IEEE Transactions on Circuits and Systems*, vol. 32, no. 10, pp. 1041–1049, 1985.
- [10] M. Jan, B. Janusz, and B. Jim, *Power system dynamics: stability and control, 2nd Edition*. Wiley, 2008.
- [11] J. H. Chow, G. E. Boukarim, and A. Murdoch, “Power system stabilizers as undergraduate control design projects,” *IEEE Transactions on power systems*, vol. 19, no. 1, pp. 144–151, 2004.
- [12] I. Hiskens and J. Milanovic, “Load modelling in studies of power system damping,” *IEEE Transactions on Power Systems*, vol. 10, no. 4, pp. 1781–1788, 1995.
- [13] D. J. Hill, “Nonlinear dynamic load models with recovery for voltage stability studies,” *IEEE Transactions on Power Systems*, vol. 8, no. 1, pp. 166–176, 1993.
- [14] C. Sloth, T. Esbensen, and J. Stoustrup, “Active and passive fault-tolerant LPV control of wind turbines,” in *Proc. of American Control Conference*, 2010, pp. 4640–4646.
- [15] C. E. Ugalde-Loo, J. B. Ekanayake, and N. Jenkins, “State-space modeling of wind turbine generators for power system studies,” *IEEE Transactions on Industry Applications*, vol. 49, no. 1, pp. 223–232, 2013.
- [16] A. Ortega and F. Milano, “Generalized model of vsc-based energy storage systems for transient stability analysis,” *IEEE Transactions on Power Systems*, vol. 31, no. 5, pp. 3369–3380, 2016.
- [17] O. Anaya-Lara, D. Campos-Gaona, E. Moreno-Goytia, and G. Adam, *Offshore Wind Energy Generation: Control, Protection, and Integration to Electrical Systems*. John Wiley & Sons, 2014.
- [18] H. J. Sira-Ramirez and R. Silva-Ortigoza, *Control design techniques in power electronics devices*. Springer Science & Business Media, 2006.
- [19] M. G. Villalva, J. R. Gazoli, and E. Ruppert Filho, “Comprehensive approach to modeling and simulation of photovoltaic arrays,” *IEEE Transactions on Power Electronics*, vol. 24, no. 5, pp. 1198–1208, 2009.
- [20] C. Canizares *et al.*, “Benchmark systems for small-signal stability analysis and control,” *IEEE Power and Energy Society Technical report*, 2015.
- [21] T. Sadamoto, *MATLAB codes used for the simulations*, 2018, available at: <https://github.com/TSadamoto/CSM2018>.
- [22] P. W. Sauer, M. A. Pai, and J. H. Chow, *Power System Dynamics and Stability: With Synchrophasor Measurement and Power System Toolbox*. John Wiley & Sons, 2017.

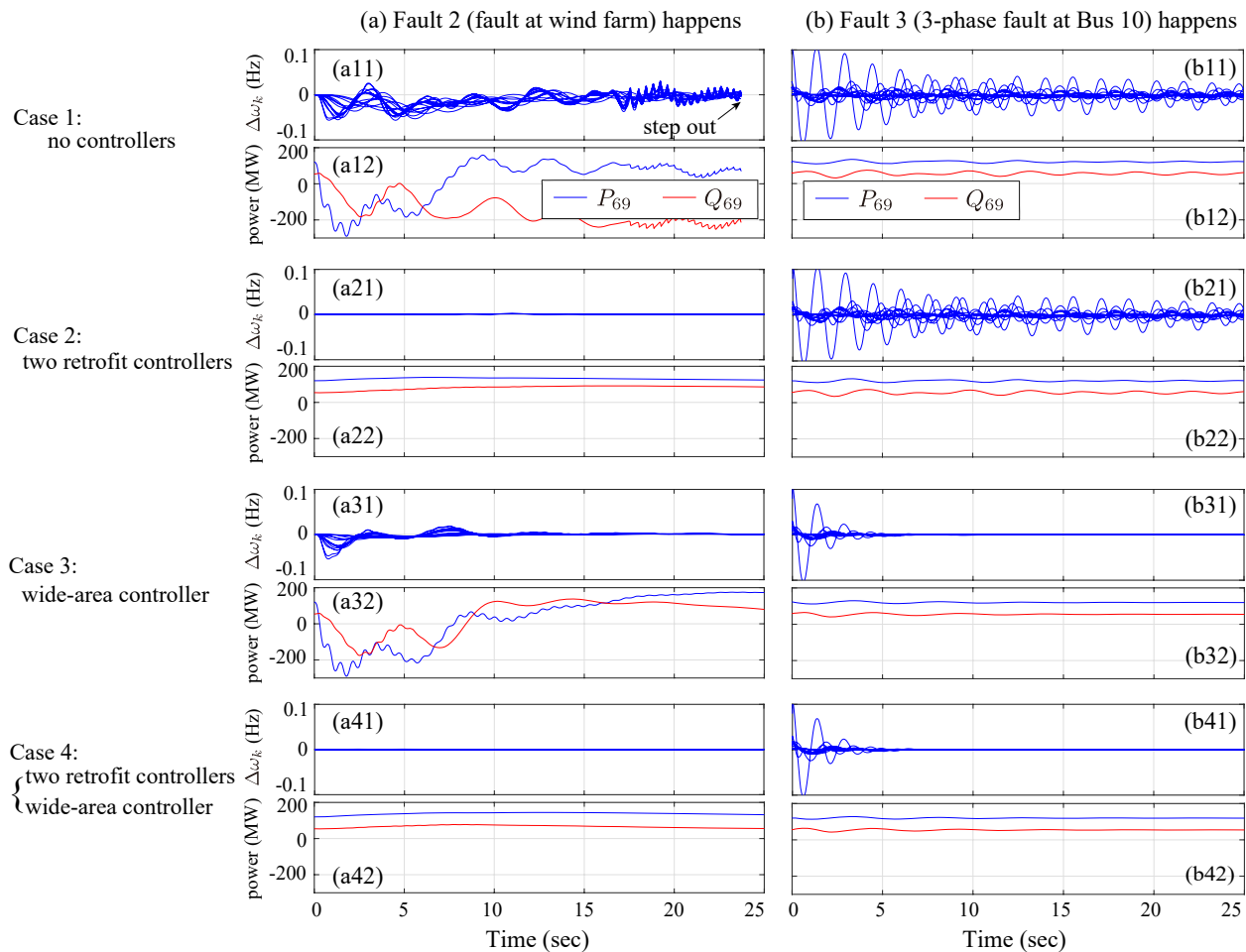


Fig. 22. Trajectories of the frequency deviation of all synchronous generators and power injecting from the wind farm when (top two panels) no additional controllers, (second two panels) two retrofit controllers, (third two panels) wide-area controller, and (bottom two panels) both of the two retrofit controllers and the wide-area controllers are used, respectively, for (left column) the fault at the wind farm and (right column) three-phase fault at Bus 10.

- [23] T. Sadamoto, A. Chakraborty, T. Ishizaki, and J. Imura, "Retrofit control of wind-integrated power systems," *IEEE Transactions on Power Systems*, vol. 33, no. 3, pp. 2804–2815, 2018.
- [24] S. Wang, X. Meng, and T. Chen, "Wide-area control of power systems through delayed network communication," *IEEE Transactions on Control Systems Technology*, vol. 20, no. 2, pp. 495–503, 2012.
- [25] D. Soudbakhsh, A. Chakraborty, and A. M. Annaswamy, "A delay-aware cyber-physical architecture for wide-area control of power systems," *Control Engineering Practice*, vol. 60, pp. 171–182, 2017.
- [26] Y.-F. Huang, S. Werner, J. Huang, N. Kashyap, and V. Gupta, "State estimation in electric power grids: Meeting new challenges presented by the requirements of the future grid," *IEEE Signal Processing Magazine*, vol. 29, no. 5, pp. 33–43, 2012.
- [27] E. Ghahremani and I. Kamwa, "Dynamic state estimation in power system by applying the extended kalman filter with unknown inputs to phasor measurements," *IEEE Transactions on Power Systems*, vol. 26, no. 4, pp. 2556–2566, 2011.
- [28] E. Farantatos, G. K. Stefopoulos, G. J. Cokkinides, and A. Meliopoulos, "PMU-based dynamic state estimation for electric power systems," in *Proc. of IEEE Power & Energy Society General Meeting*, 2009, pp. 1–8.
- [29] M. B. Do Coutto Filho and J. C. S. de Souza, "Forecasting-aided state estimation-part i: Panorama," *IEEE Transactions on Power Systems*, vol. 24, no. 4, pp. 1667–1677, 2009.
- [30] F. Lin, M. Fardad, and M. R. Jovanović, "Design of optimal sparse feedback gains via the alternating direction method of multipliers," *IEEE Transactions on Automatic Control*, vol. 58, no. 9, pp. 2426–2431, 2013.
- [31] R. Yousefian, R. Bhattarai, and S. Kamalasan, "Direct intelligent wide-area damping controller for wind integrated power system," in *Proc. of IEEE Power and Energy Society General Meeting*, 2016, pp. 1–5.
- [32] F. P. Demello and C. Concordia, "Concepts of synchronous machine stability as affected by excitation control," *IEEE Transactions on Power Apparatus and Systems*, vol. 88, no. 4, pp. 316–329, 1969.
- [33] G. J. Dudgeon, W. E. Leithead, A. Dysko, J. o'Reilly, and J. R. McDonald, "The effective role of AVR and PSS in power systems: Frequency response analysis," *IEEE Transactions on Power Systems*, vol. 22, no. 4, pp. 1986–1994, 2007.

- [34] I. P. E. Society, "IEEE recommended practice for excitation system models for power system stability studies," *IEEE Standard 421.5*, 2005.
- [35] Y. Chen, "Decentralized robust control design for large-scale uncertain systems: The uncertainty is time-varying," *Journal of the Franklin Institute*, vol. 329, no. 1, pp. 25–36, 1992.
- [36] Y. Chen and H. MC, "Decentralized control design for interconnected uncertain systems," *Control and Dynamic Systems*, vol. 56, no. 2, pp. 219–266, 1993.
- [37] P. Moylan and D. Hill, "Stability criteria for large-scale systems," *IEEE Transactions on Automatic Control*, vol. 23, no. 2, pp. 143–149, 1978.
- [38] Z. Qu and M. A. Simaan, "Modularized design for cooperative control and plug-and-play operation of networked heterogeneous systems," *Automatica*, vol. 50, no. 9, pp. 2405–2414, 2014.
- [39] C. Zhao and S. Low, "Optimal decentralized primary frequency control in power networks," in *Proc. of Conference on Decision and Control*, 2014, pp. 2467–2473.
- [40] G. Rinaldi, M. Cucuzzella, and A. Ferrara, "Third order sliding mode observer-based approach for distributed optimal load frequency control," *IEEE Control Systems Letters*, vol. 1, no. 2, pp. 215–220, 2017.
- [41] H. Bevrani, *Robust power system frequency control*. Springer, 2009, vol. 85.
- [42] Y. Wang, D. J. Hill, and G. Guo, "Robust decentralized control for multimachine power systems," *IEEE Transactions on Circuits and Systems I: Fundamental Theory and Applications*, vol. 45, no. 3, pp. 271–279, 1998.
- [43] D. D. Siljak, D. M. Stipanovic, and A. I. Zecevic, "Robust decentralized turbine/governor control using linear matrix inequalities," *IEEE Transactions on Power Systems*, vol. 17, no. 3, pp. 715–722, 2002.
- [44] H. Cai, Z. Qu, and J. F. Dorsey, "Robust decentralized excitation control for large scale power systems," in *Proc. of IFAC World Congress*, vol. 29, no. 1, 1996, pp. 7058–7063.
- [45] Y. Guo, D. J. Hill, and Y. Wang, "Nonlinear decentralized control of large-scale power systems," *Automatica*, vol. 36, no. 9, pp. 1275–1289, 2000.
- [46] A. I. Zecevic, G. Neskovic, and D. D. Siljak, "Robust decentralized exciter control with linear feedback," *IEEE Transactions on Power Systems*, vol. 19, no. 2, pp. 1096–1103, 2004.
- [47] A. H. Etemadi, E. J. Davison, and R. Iravani, "A decentralized robust control strategy for multi-der microgrids-part I: Fundamental concepts," *IEEE Transactions on Power Delivery*, vol. 27, no. 4, pp. 1843–1853, 2012.
- [48] S. Fiaz, D. Zonetti, R. Ortega, J. M. Scherpen, and A. Van der Schaft, "A port-hamiltonian approach to power network modeling and analysis," *European Journal of Control*, vol. 19, no. 6, pp. 477–485, 2013.
- [49] Y. Wang, D. Cheng, C. Li, and Y. Ge, "Dissipative hamiltonian realization and energy-based L_2 -disturbance attenuation control of multimachine power systems," *IEEE Transactions on Automatic Control*, vol. 48, no. 8, pp. 1428–1433, 2003.
- [50] R. Lozano, B. Brogliato, O. Egeland, and B. Maschke, *Dissipative systems analysis and control: theory and applications*. Springer Science & Business Media, 2013.
- [51] F. Wu, X. P. Zhang, P. Ju, and M. J. Sterling, "Decentralized nonlinear control of wind turbine with doubly fed induction generator," *IEEE Transactions on Power Systems*, vol. 23, no. 2, pp. 613–621, 2008.
- [52] H. Liang, B. J. Choi, W. Zhuang, and X. Shen, "Stability enhancement of decentralized inverter control through wireless communications in microgrids," *IEEE Transactions on Smart Grid*, vol. 4, no. 1, pp. 321–331, 2013.
- [53] A. C. Zolotas, B. Chaudhuri, I. M. Jaimoukha, and P. Korba, "A study on LQG/LTR control for damping inter-area oscillations in power systems," *IEEE Transactions on Control Systems Technology*, vol. 15, no. 1, 2007.
- [54] N. R. Chaudhuri, D. Chakraborty, and B. Chaudhuri, "Damping control in power systems under constrained communication bandwidth: A predictor corrector strategy," *IEEE Transactions on Control Systems Technology*, vol. 20, no. 1, pp. 223–231, 2012.
- [55] R. A. Jabr, B. C. Pal, and N. Martins, "A sequential conic programming approach for the coordinated and robust design of power system stabilizers," *IEEE Transactions on Power Systems*, vol. 25, no. 3, pp. 1627–1637, 2010.
- [56] A. Jain, E. Biyik, and A. Chakraborty, "A model predictive control design for selective modal damping in power systems," in *Proc. of American Control Conference*, 2015, pp. 4314–4319.
- [57] M. Zima, M. Larsson, P. Korba, C. Rehtanz, and G. Andersson, "Design aspects for wide-area monitoring and control systems," *Proceedings of the IEEE*, vol. 93, no. 5, pp. 980–996, 2005.
- [58] J. H. Chow and S. G. Ghiocel, "An adaptive wide-area power system damping controller using synchrophasor data," in *Control and Optimization Methods for Electric Smart Grids*. Springer, 2012, pp. 327–342.
- [59] S. Zhang and V. Vittal, "Design of wide-area power system damping controllers resilient to communication failures," *IEEE Transactions on Power Systems*, vol. 28, no. 4, pp. 4292–4300, 2013.
- [60] R. Deng, G. Xiao, R. Lu, H. Liang, and A. V. Vasilakos, "False data injection on state estimation in power systems—attacks, impacts, and defense: A survey," *IEEE Transactions on Industrial Informatics*, vol. 13, no. 2, pp. 411–423, 2017.
- [61] A. Heniche and I. Karnwa, "Control loops selection to damp inter-area oscillations of electrical networks," *IEEE Transactions on Power Systems*, vol. 17, no. 2, pp. 378–384, 2002.
- [62] F. Dörfler, M. R. Jovanović, M. Chertkov, and F. Bullo, "Sparsity-promoting optimal wide-area control of power networks," *IEEE Transactions on Power Systems*, vol. 29, no. 5, pp. 2281–2291, 2014.
- [63] A. R. Bergen and D. J. Hill, "A structure preserving model for power system stability analysis," *IEEE Transactions on Power Apparatus and Systems*, no. 1, pp. 25–35, 1981.
- [64] S. Chandra, D. F. Gayme, and A. Chakraborty, "Time-scale modeling of wind-integrated power systems," *IEEE Transactions on Power Systems*, vol. 31, no. 6, pp. 4712–4721, 2016.

A. A Brief Survey on Control of Synchronous Generators

Control of synchronous generators is generally classified into two groups: prime mover control and excitation system control [6]. The former aims at balancing the total system generation against system load and losses so that the desired frequency and power interchange are maintained. These controllers are further subdivided into *primary, secondary, and tertiary control*; for details see [10]. However, the prime-mover control is usually much slower than the time-scale of oscillation damping, and, therefore, is not discussed in this article. The excitation system control, on the other hand, is achieved by Automatic Voltage Regulator (AVR) for the regulation of voltage and reactive power, as well as by Power System Stabilizer (PSS) for the enhancement of power system stability and damping of power flow oscillations [6]. A long line of work exists for AVR/PSS design using tools from control theory - for example, see [7], [11], [22], [32], [33], [34]. In today's grid, many of these controllers are being executed using real-time measurements from Phasor Measurement Units (PMUs) [2], integrated with efficient state estimation techniques such as *forecasting-aided state estimation* [26], [27], [28], [29].

B. A Brief Survey on Local Control of Power Systems

Local control of power systems relies on two main techniques - decentralized robust control [35], [36] and dissipativity-based control [37], [38]. Applications of these two methods to power systems can be found in papers such as [39], [40], [41], [42], [43], [44], [45], [46], [47] for the former, and [48], [49] for the latter. However, these methods have the following drawbacks. One drawback is that the class of applicable systems is restrictive. In the decentralized robust control, interferences among generators are regarded as norm-bounded uncertainty, and a stabilizing controller for any of the uncertainties are designed. Thus, basically, this approach is applicable to weakly-coupled systems. Power system models, in general, however do not fall in this category. The dissipativity-based control is limited to dissipative network systems only. Although conventional synchronous generator models satisfy this property, the approach cannot be easily extended to DER models. In fact, the papers [48], [49] deal with multi-machine power systems without DERs. Another drawback is that these methods need a priori knowledge of the entire system model. For example, in the decentralized robust control, a small-gain type property bounded by the uncertainties, which cannot be computed without using an entire network system model, is required. On the other hand, in dissipativity-based control, the interconnection among subsystems should be appropriate such that the networked system is stable [50]. However, the design of this interconnection structure is difficult to perform by local subsystem information.

In contrast, the retrofit control proposed in [4] is applicable to a much more general class of stable systems that do not require any of the above specifications. The design and implementation can be done independently from the information of any other grid components, that is, the retrofit controller has a plug-and-play capability. Moreover, in contrast to heuristic tuning of local controllers as presented in literature [51], [52], this method can theoretically guarantee the overall closed-loop system stability; details are described in the section Section IV-A.

C. A Brief Survey on Wide-Area Control

Recent papers have proposed the design of WAC for power oscillation damping based on optimal control [53], [54], LMIs and conic programming [55], model predictive control [56], model reduction and control inversion [57], and adaptive control [58]. A tutorial on these different methods has recently been reported in [3]. The paper [59] has proposed wide-area control that can be resilient to failures. One drawback of these methods is that they usually result in a centralized implementation that can be computationally challenging. Centralized control is also not very resilient to cyber-attacks [59], [60]. Thus, in recent years, power system operators are inclining more towards distributed wide-area control, where the communication graph among controllers is sparse [61], [62]. The work in [61] uses geometric measures for selection of control loops, whereas [62] uses a sparsity-promoting LQR-based optimal control strategy. LQR is often

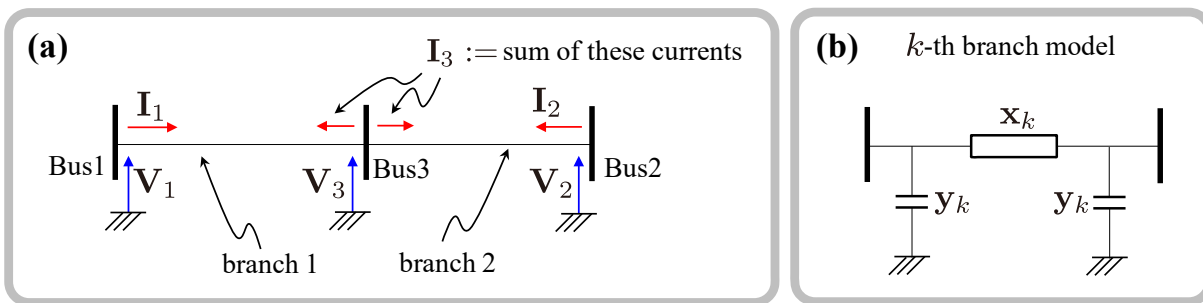


Fig. 23. (a) Simple power system consisting of three buses. (b) The k -th branch model so-called Π -type circuit.

chosen as the central design tool as it provides flexibility in damping selected ranges of frequencies. A real-time version of the sparse LQR design has been proposed in [5] using spectral decomposition of online PMU measurements. An advantage of this method over [62], [61] is that this approach can provide sparser wide-area controllers than those methods, with a comparable closed-loop performance; please see [5] for more detailed discussion of this point based on numerical simulations.

A brief tutorial of constructing the admittance matrix \mathbf{Y} from tie-line data typically shown in literature, for example [7] is described. For this purpose, a power network consisting of three buses, as shown in Figure 23 (a), is considered, where \mathbf{V}_k is the k -th bus voltage and \mathbf{I}_k is the current injected from the bus. Typically, each branch is modeled as a so-called Π -type circuit as shown in Figure 23 (b), where \mathbf{x}_k is the branch impedance and \mathbf{y}_k is the shunt admittance representing a capacitance between the transmission line and ground. The values of \mathbf{x}_k and \mathbf{y}_k for all branches are given data.

The bus voltage and current must satisfy Kirchoff's law, that is,

$$\mathbf{I}_{1:3} = \mathbf{Y}\mathbf{V}_{1:3}, \quad \mathbf{I}_{1:3} := [\mathbf{I}_1, \mathbf{I}_2, \mathbf{I}_3]^\top, \quad \mathbf{V}_{1:3} := [\mathbf{V}_1, \mathbf{V}_2, \mathbf{V}_3]^\top, \quad (50)$$

where $\mathbf{Y} \in \mathbb{C}^{3 \times 3}$ is the admittance matrix. Note that (50) is equivalent to (2) when $N = 3$ by taking conjugate of (50) and multiplying each k -th row of (50) by \mathbf{V}_k . Thus, \mathbf{Y} in (50) is the matrix that needs to be constructed. The calculation of its (1,1)-element, denoted by \mathbf{Y}_{11} , is as follows. Note that (50) should hold in a special case when $\mathbf{V}_2 = \mathbf{V}_3 = 0$. Then, the first line in (50) becomes $\mathbf{I}_1 = \mathbf{Y}_{11}\mathbf{V}_1$. On the other hand, when $\mathbf{V}_2 = \mathbf{V}_3 = 0$, it follows from Figure 23 (a) that $\mathbf{I}_1 = (\mathbf{y}_1 + \mathbf{x}_1^{-1})\mathbf{V}_1$. Thus, $\mathbf{Y}_{11} = \mathbf{y}_1 + \mathbf{x}_1^{-1}$. Repeating this for all elements, the admittance matrix is constructed as

$$\mathbf{Y} = \begin{bmatrix} \mathbf{y}_1 + \mathbf{x}_1^{-1} & 0 & -\mathbf{x}_1^{-1} \\ 0 & \mathbf{y}_2 + \mathbf{x}_2^{-1} & -\mathbf{x}_2^{-1} \\ -\mathbf{x}_1^{-1} & -\mathbf{x}_2^{-1} & \mathbf{y}_1 + \mathbf{y}_2 + \mathbf{x}_1^{-1} + \mathbf{x}_2^{-1} \end{bmatrix}. \quad (51)$$

D. Brief Tutorial on Power Flow Calculation

Given the number of buses N and an admittance matrix \mathbf{Y} , the power flow calculation, namely a procedure of finding bus voltage \mathbf{V}_k^* , active power P_k^* , and reactive power Q_k^* for $k \in \{1, \dots, N\}$ satisfying

$$0 = (\mathbf{Y}\mathbf{V}_{1:N}^*)^* \circ \mathbf{V}_{1:N}^* - (P_{1:N}^* + jQ_{1:N}^*), \quad \begin{cases} \mathbf{V}_{1:N}^* := [\mathbf{V}_1^* \cdots \mathbf{V}_N^*]^\top, \\ P_{1:N}^* + jQ_{1:N}^* := [P_1^* + jQ_1^* \cdots P_N^* + jQ_N^*]^\top, \end{cases} \quad (52)$$

where \circ is the element-wise multiplication and $*$ is the element-wise complex conjugate operator, is explained. Note that there exist $4N$ decision variables, namely P_k^* , Q_k^* and both the magnitude and angle of \mathbf{V}_k^* for $k \in \{1, \dots, N\}$, while (52) consists of $2N$ algebraic constraints, namely its real part and imaginary part. Hence, there exist an infinite number of solutions satisfying (52). In order to choose a practical solution, $2N$ additional constraints reflecting component characteristics are typically considered in addition to (52). In this setting, a standard power flow calculation is formulated as follows.

Given a natural number N and $\mathbf{Y} \in \mathbb{C}^{N \times N}$ and $h_k(\cdot, \cdot, \cdot) : \mathbb{C} \times \mathbb{R} \times \mathbb{R} \rightarrow \mathbb{C}$ for $k \in \{1, \dots, N\}$, find \mathbf{V}_k^* , P_k^* and Q_k^* satisfying (52) and

$$0 = h_k(\mathbf{V}_k^*, P_k^*, Q_k^*), \quad \text{for } k \in \{1, \dots, N\}. \quad (53)$$

The detail of the additional constraint $h_k(\cdot, \cdot, \cdot)$ for generators, loads, non-unit buses, wind farms, solar farms, and energy storage systems are described below. Let $\mathbb{N}_G, \mathbb{N}_L, \mathbb{N}_W, \mathbb{N}_S, \mathbb{N}_E, \mathbb{N}_N$ be the index sets of the buses connecting to generators, loads, wind farms, solar farms, energy storages, and that of non-unit buses. Those sets are supposed to be disjoint, and $\mathbb{N}_G \cup \mathbb{N}_L \cup \mathbb{N}_W \cup \mathbb{N}_S \cup \mathbb{N}_E \cup \mathbb{N}_N = \{1, \dots, N\}$.

The non-unit buses must satisfy

$$0 = P_k^* + jQ_k^*, \quad k \in \mathbb{N}_N. \quad (54)$$

For the loads and energy storage systems, their steady-state active/reactive power $\bar{P}_k + j\bar{Q}_k$, is known in advance. In view of this, $h_k(\cdot, \cdot, \cdot)$ for those units is

$$0 = P_k^* + jQ_k^* - (\bar{P}_k + j\bar{Q}_k), \quad k \in \mathbb{N}_L \cup \mathbb{N}_E. \quad (55)$$

The buses associated with $\mathbb{N}_N, \mathbb{N}_L$, and \mathbb{N}_E are called *PQ-buses* because the steady-state values of their active (P) and reactive (Q) power are given for the power flow calculation. For wind farms, solar farms and generators, their steady-state active power and bus voltage magnitude are usually known. However, because the power loss through the transmission lines are not known a priori, active and reactive power of at least one component must be unspecified. Let this component be the generator connecting to the k_s -th bus for a given $k_s \in \mathbb{N}_G$, and assume

$$0 = |\mathbf{V}_{k_s}^*| - \bar{V}_{k_s}, \quad 0 = \angle \mathbf{V}_{k_s}^* - \bar{\theta}_{k_s}, \quad (56)$$

for given $\bar{V}_{k_s} \in \mathbb{R}$ and $\bar{\theta}_{k_s} \in \mathbb{R}$. Without loss of generality, $\bar{\theta}_{k_s} = 0$. The k_s -th bus is called the *slack bus*, or sometimes *swing bus*. The other generators, wind farms, and solar farms are assumed to satisfy

$$0 = P_k^* - \bar{P}_k, \quad 0 = |\mathbf{V}_k^*| - \bar{V}_k, \quad k \in \mathbb{N}_G \cup \mathbb{N}_W \cup \mathbb{N}_S \setminus \{k_s\}, \quad (57)$$

for given $\bar{P}_k \in \mathbb{R}$ and $\bar{V}_k \in \mathbb{R}$. The buses associated with $\mathbb{N}_N, \mathbb{N}_L$, and \mathbb{N}_E are called *PV-buses* because their steady-state values of the active (P) power and voltage magnitude (V) are given for the power flow calculation.

Finally, the power flow calculation is summarized as follows. Find $\mathbf{V}_{1:N}^*$, $P_{1:N}^*$ and $Q_{1:N}^*$ satisfying (52) and (54), (55), (56), and (57). This is what exactly done in the **Power Flow Calculation** step described in Section II.

E. Relationship between the Standard Models of a Synchronous Machine

Four standard models of a synchronous machine are commonly used in power system modeling, depending of the desired resolution of the model [6]. These models are called the *Park model*, the *sub-transient model*, the *one-axis model*, and the *classical model*. The mathematical relationship among these models is summarized here. The Park model is one of the most well-known synchronous machine model, which is the combination of the motion dynamics and the electro-magnetic dynamics representing the flux variation of d- and q-axis circuits, excitation winding, and some amortisseur windings. The equations of those two dynamics can be found in Sections 3.9 and 3.4.9 in [6], respectively. Assuming that the d- and q-axis circuit flux dynamics are sufficiently fast, the Park model can be simplified to the *sub-transient model* with four coils on the rotor [7]. The model consists of the motion dynamics (a second-order system) and the fourth-order system representing flux variation of excitation windings, one d-axis amortisseur winding, and two q-axis amortisseur windings. By further assuming that the amortisseur effects are negligible and the resistance between the generator and its connecting bus is negligible, the sub-transient model can then be simplified to (4)-(5). This model is called the *one-axis model* [8], [63] in the sense that its electro-magnetic dynamics represent the flux variation of only the excitation winding. In [64], a further simplified

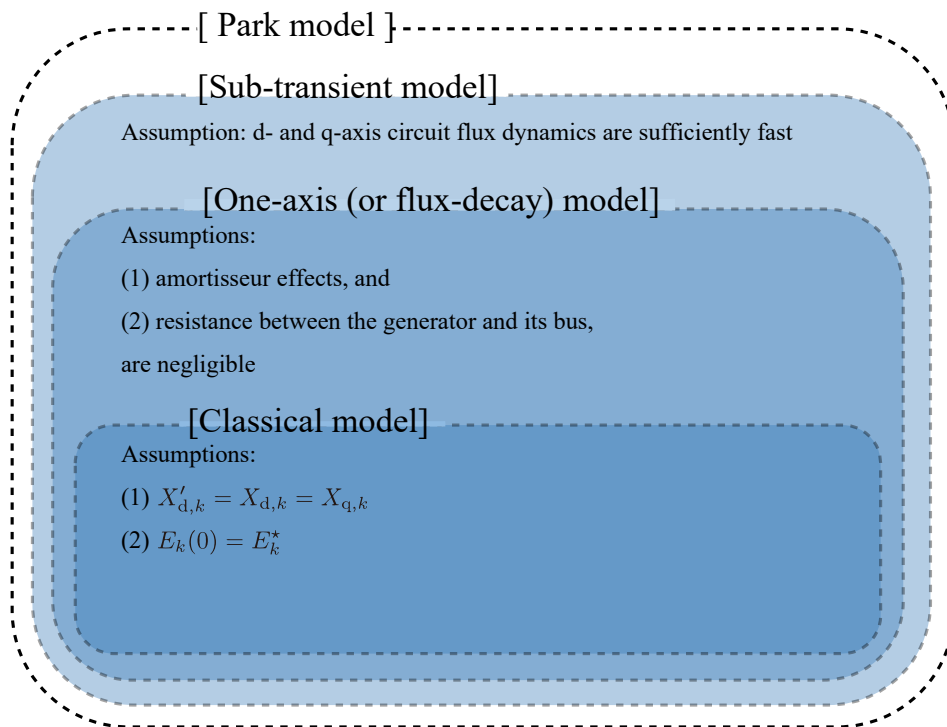


Fig. 24. Relationship among four standard synchronous machine models

one-axis model under the assumption $X_{q,k} = X'_{d,k}$ in (4)-(5) is presented. When $X_{d,k} = X_{q,k}$, which can be satisfied for round rotor machines due to the symmetrical air gap between d- and q-axes [10], the electro-magnetic dynamics of the simplified one-axis model is reduced to $\tau_{do,k} \dot{E}_k = -E_k + V_{fd,k}$. Thus, supposing that the initial value of the internal voltage E_k is its steady-state value E_k^* and $V_{fd,k}(t) \equiv E_k^*$, it clearly follows that $E_k(t) \equiv E_k^*$ for all t . In that case, the simplified one-axis model can be simply written as

$$\left\{ \begin{array}{l} \dot{\delta}_k = \bar{\omega} \Delta \omega_k, \\ \Delta \dot{\omega}_k = \frac{1}{M_k} \left(P_{m,k} - d_k \Delta \omega_k - \frac{|\mathbf{V}_k| E_k^*}{X_{d,k}} \sin(\delta_k - \angle \mathbf{V}_k) \right), \\ P_k + jQ_k = \frac{E_k^* |\mathbf{V}_k|}{X_{d,k}} \sin(\delta_k - \angle \mathbf{V}_k) + j \left(\frac{E_k^* |\mathbf{V}_k|}{X_{d,k}} \cos(\delta_k - \angle \mathbf{V}_k) - |\mathbf{V}_k|^2 \right). \end{array} \right. \quad (58)$$

This model is called the *classical model* [6], [10]. The relationship among the four models is shown in Figure 24.